Saharan Dust and the Nonlinear Evolution of the African Easterly Jet–African Easterly Wave System

DUSTIN F. P. GROGAN

Department of Atmospheric and Environmental Sciences, University at Albany, State University of New York, Albany, New York

TERRENCE R. NATHAN AND SHU-HUA CHEN

Atmospheric Science Program, Department of Land, Air, and Water Resources, University of California, Davis, Davis, California

(Manuscript received 19 April 2016, in final form 2 September 2016)

ABSTRACT

The direct radiative effects of Saharan mineral dust (SMD) aerosols on the nonlinear evolution of the African easterly jet–African easterly wave (AEJ–AEW) system is examined using the Weather Research and Forecasting Model coupled to an online dust model. The SMD-modified AEW life cycles are characterized by four stages: enhanced linear growth, weakened nonlinear stabilization, larger peak amplitude, and smaller long-time amplitude. During the linear growth and nonlinear stabilization stages, the SMD increases the generation of eddy available potential energy (APE); this occurs where the maximum in the mean meridional SMD gradient is coincident with the critical surface. As the AEWs evolve beyond the nonlinear stabilization stage, the discrimination between SMD particle sizes due to sedimentation becomes more pronounced; the finer particles meridionally expand, while the coarser particles settle to the surface. The result is a reduction in the eddy APE at the base and the top of the plume.

The SMD enhances the Eliassen–Palm (EP) flux divergence and residual-mean meridional circulation, which generally oppose each other throughout the AEW life cycle. The SMD-modified residual-mean meridional circulation initially dominates to accelerate the flow but quickly surrenders to the EP flux divergence, which causes an SMD-enhanced deceleration of the AEJ during the linear growth and nonlinear stabilization stages. Throughout the AEW life cycle, the SMD-modified AEJ is elevated and the peak winds are larger than without SMD. During the first (second) half of the AEW life cycle, the SMD-modified wave fluxes shift the AEJ axis farther equatorward (poleward) of its original SMD-free position.

1. Introduction

The African easterly jet (AEJ) and African easterly waves (AEWs) characterize the summertime meteorology over North Africa and the eastern Atlantic Ocean. The AEJ and AEWs together form a complicated nonlinear system, wherein barotropic–baroclinic instability of the AEJ provides energy for the growth of the AEWs, while the heat and momentum fluxes of the AEWs feedback on the AEJ to affect its strength and structure (Burpee 1972; Thorncroft and Hoskins 1994a,b; Hseih and Cook 2005).

The nonlinear evolution of the AEJ–AEW system is further complicated by the direct radiative effects[1] of Saharan mineral dust (SMD) aerosols, which are emitted by localized sources over North Africa (Engelstaedter and Washington 2007; Knippertz and Todd 2012). Nocturnal jets, boundary layer convection, and AEWs are among the circulation features that form synoptic-scale plumes of SMD (Jones et al. 2003; Cuesta et al. 2009; Knippertz and Todd 2012; Fielder et al. 2013). The plumes affect the surface and atmospheric energy budgets (Miller and Tegen 1998), which in turn alter the circulation and transport of the SMD (Jones

Corresponding author address: Dustin Grogan, Department of Atmospheric and Environmental Sciences, 1400 Washington Ave., University at Albany, State University of New York, Albany, NY 12222.
E-mail: dgrogan@albany.edu

[1] The direct radiative effects of SMD involve changes in the energy budget due to absorption, emission, and scattering of radiation.

DOI: 10.1175/JAS-D-16-0118.1

et al. 2004; Chen et al. 2010; Ma et al. 2012; Grogan et al. 2016), forming a complicated feedback loop that is continuously modulated by SMD sources and sinks.

Despite the complexities in modeling and identifying the feedbacks operating within the SMD-modified AEJ–AEW system, important advances have been made. For example, Tompkins et al. (2005), Reale et al. (2011), Chen et al. (2010), and Colarco et al. (2014), among others, have shown that the SMD can significantly affect the AEJ. Although these studies used different models, datasets, or both, there is one overarching finding for which they agree: the SMD affects the thermal field, which, via the thermal wind balance, changes the strength and structure of the AEJ. Tompkins et al. (2005), for example, compared 4 months of ECMWF 5-day forecasts using two generations of global SMD climatologies. One generation was based on an annual-average aerosol optical depth (AOD) distribution, while the other was based on monthly mean distributions. Tompkins et al. (2005) showed that the direct radiative effects of monthly varying SMD, which is a more realistic representation, positioned the AEJ farther south and increased the zonal velocity on its southern flank. These SMD-induced changes resulted in AEJ forecasts that were in closer agreement with the ECMWF analyses.

In contrast to the AEJ, where the SMD-modified thermal wind is invoked to explain the changes in the strength and structure of the AEJ, the effects of SMD on AEWs are less clear. For instance, the modeling studies of Karyampudi and Carlson (1988) and Jury and Santiago (2010) show that SMD can weaken AEWs, whereas Jones et al. (2004), Ma et al. (2012), and Grogan et al. (2016) show that SMD can strengthen AEWs. Hosseinpour and Wilcox (2014) show that SMD can either strengthen or weaken the growth of AEWs depending on their position relative to the SMD field.

Grogan et al. (2016) provided a comprehensive discussion of the possible reasons for the differences in how the AEWs respond to SMD. The reasons include differences in the locations of the plumes relative to the AEJ and differences in the meridional and vertical distributions of SMD. Regarding the latter, the SMD distributions differ markedly between North Africa, where the SMD is well mixed in the boundary layer, and the eastern Atlantic, where the SMD plumes are lofted above the cool, moist marine layer to form the Saharan air layer.

To help explain how the location and distribution of the SMD relative to the AEJ affect the growth and structure of AEWs, Grogan et al. (2016) used a linearized version of the Weather Research and Forecasting (WRF) Model coupled to an online dust model. Focusing on North Africa, where the SMD plumes and AEWs both originate, Grogan et al. (2016) carried out a linear stability analysis of a zonally averaged background state, where the distributions of wind, temperature, and SMD were chosen consistent with observations. The numerical results showed that the direct radiative effects of the SMD increased the linear growth rates of the AEWs by ~5%–20%. Using an analytically derived expression for the SMD-modified, local generation of eddy APE, Grogan et al. (2016) were able to explain the physics and confirm through the numerical experiments that the generation of eddy APE is largest where the maximum in the meridional SMD gradient coincides with the critical surface—that is, where the Doppler-shifted frequency vanishes in the latitude–height plane.

The purpose of this study is to extend Grogan et al. (2016) by considering the direct radiative effects of the SMD on the nonlinear evolution of the AEJ–AEW system. Emphasis is placed on determining the effects of the SMD on the structural evolution of the AEJ and the life cycles of the model's AEWs. Our study is guided in part by Thorncroft and Hoskins (1994b), who examined in a dust-free model the nonlinear evolution of the AEJ–AEW system. Using domain-averaged energetics and Eliassen–Palm (EP) flux diagnostics, Thorncroft and Hoskins (1994b) characterized the evolution of the AEWs by four stages: initial linear growth, reduced growth due to stabilization of the AEJ by zonally averaged wave fluxes, peak wave amplitude, and reduction and eventual equilibration of the wave amplitude.

Given the four-stage AEW evolution identified by Thorncroft and Hoskins (1994b) for a SMD-free system, several questions emerge. How will the SMD affect each stage, particularly the timing and value of the peak amplitude? How will the SMD-modified wave driving combined with the zonally averaged SMD heating affect the speed, location, and structure of the AEJ? And how will different SMD particle sizes, which constitute the plume and its radiative effects, affect the evolution of the eddy APE throughout the life cycles of the AEWs? These questions, among others, will be addressed through a sequence of carefully designed experiments and diagnostics, which will be interpreted using a model equation for nonlinear wave evolution.

2. Model and initial states

As in Grogan et al. (2016), we use an idealized version of the model developed by Chen et al. (2015), which couples the WRF Model to an online dust model. The dust model consists of 12 continuity equations, with each equation corresponding to a different dust particle size

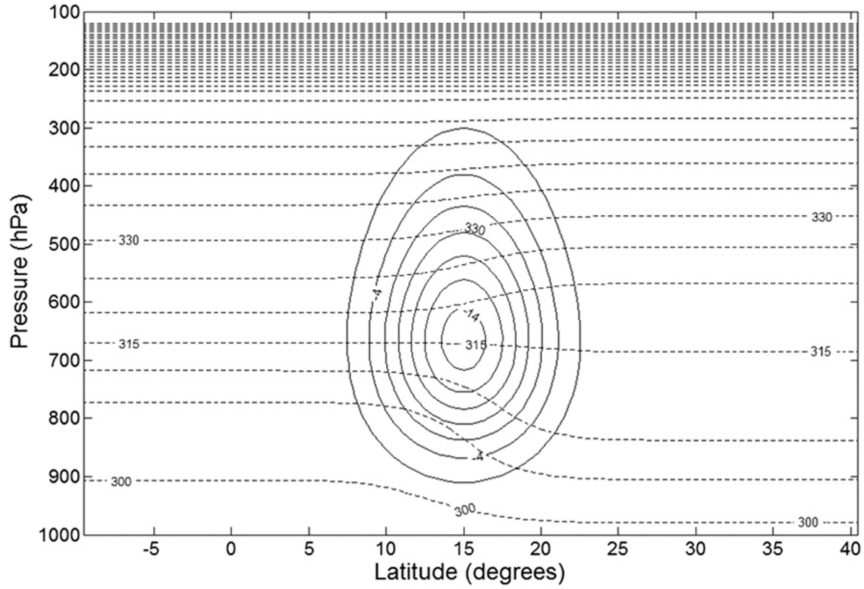

FIG. 1. Initial background distributions of zonally averaged wind (solid; m s^{-1}) and potential temperature (dashed; K). Contour intervals are 2 m s^{-1} for wind and 5 K for temperature.

(radii ranging from 0.15 to 5 μm). The dust radiative flux calculations use the NASA Goddard Space Flight Center radiation model, which accounts for shortwave heating due to dust absorption and scattering, longwave cooling due to dust, and the reabsorption of longwave radiation by other constituents (Chou and Suarez 1999; Chou et al. 2001). All other physics within the WRF–Dust model are deactivated, including boundary layer microphysics, cumulus parameterization, planetary boundary layer, and land surface processes.

The WRF–Dust model was initialized with zonally averaged distributions of wind, temperature, and SMD, upon which we superimposed a horizontal perturbation wind, with prescribed zonal wavelength of 3300 km, amplitude of 1.0 m s^{-1}, and structure that is constant in the latitude–height plane (we have found that the results are independent of the initial wave structure). The zonal wavelength corresponds to the most unstable AEW found in Grogan et al. (2016). As the model integrates forward in time, the wave grows to finite amplitude—that is, when the winds of the AEW and AEJ have similar magnitude. During growth, the initial wave interacts with itself to produce higher zonal harmonics, whose combined wave fluxes drive changes in the zonally averaged background fields. Each experiment runs for 20 days, which captures the life cycle of the AEW—its growth, peak amplitude, and eventual decay.

Figure 1 shows the initial zonally averaged wind (solid) and potential temperature (dashed) fields. The initial fields are the same as those used in Grogan et al. (2016). The zonally averaged wind represents the AEJ, which is symmetric in latitude and asymmetric in height; the jet is centered at 650 hPa and 15°N latitude and has a maximum speed of 15 m s^{-1} (Reed et al. 1977; Burpee 1972). The corresponding potential temperature field satisfies thermal wind balance.

Figure 2 shows the total SMD mass mixing ratio (solid) and the reference water vapor profile (dotted) used to compute the SMD heating rates. The structure of the SMD plume is consistent with climatological observations over the Sahara Desert (Moulin and Chiapello 2004; Konare et al. 2008). From the surface to ~750 hPa, which is the approximate height of the convective boundary layer over the Sahara, the SMD mass mixing ratio is constant (Cuesta et al. 2009). Above 750 hPa the SMD rapidly decreases up to ~650 hPa. Because observations show that the primary latitude belt for SMD emission is ~18°–22°N (Engelstaedter and Washington 2007), we initially center the plume at 20°N and choose a meridionally symmetric Gaussian distribution with a half-width of ~2.5°. The SMD mixing ratios are scaled so that the plume center (20°N) produces a maximum AOD of 1.0, which is a typical value based on observed SMD emissions over the Sahara. For very strong SMD emissions the AOD can exceed 3.0 (Tulet et al. 2008). The initial number size distribution of the SMD particles is log-normally distributed based on the dust emission observed over the Sahara (Kok 2011). Given the plume height, particle size distribution, and AOD, the maximum total SMD mixing ratio from the twelve SMD particles is ~800 μg kg^{-1}.

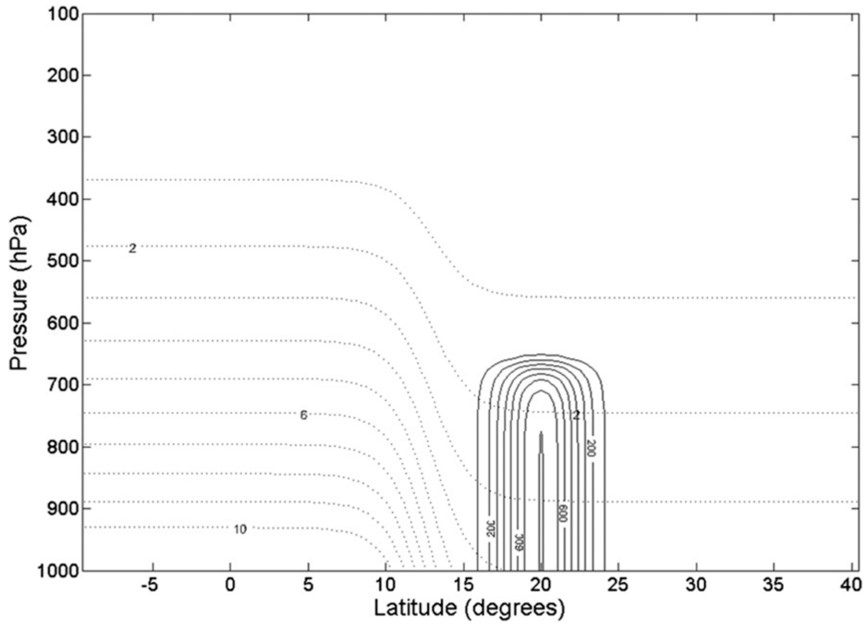

FIG. 2. Initial background SMD mass mixing ratio (solid; μg kg^{-1}) and reference water vapor profile (dotted; g kg^{-1}). The SMD mass mixing ratio includes the concentrations of all 12 SMD particle sizes. Contour intervals are 100.0 μg kg^{-1} for SMD and 1.0 g kg^{-1} for water vapor.

The evolution of each of the 12 SMD particle sizes in the model is due to the flux divergence of the SMD mixing ratio and the size-dependent particle sedimentation rate; we exclude parameterizations for subgrid cumulus and boundary layer mixing, surface emission, and wet and dry deposition. Based on the SMD distribution at each time step, the model computes the daily averaged SMD heating rate by using a declination angle of 15° and a solar zenith angle of 30.5°, which as shown in Grogan et al. (2016), produces SMD heating rates that resemble the daily averaged heating profiles in Carlson and Benjamin (1980). The zonally averaged SMD heating rates drive changes in the zonally averaged background fields; this is in contrast to the linear simulations by Grogan et al. (2016), who used prescribed forcings to ensure that the background states were fixed.

In the horizontal directions, we use a global channel projected on a cylindrical-equidistant grid that extends from 10°S to 40°N with a horizontal resolution of 0.5°. In the vertical direction, there are 50 terrain-following levels with the model top at 100 hPa; there is no bottom topography. The boundary conditions are periodic in the east–west direction, symmetric at the north and south channel walls, and free slip at the top and bottom boundaries.

3. Generation of eddy APE

In the linear study by Grogan et al. (2016), the 12 SMD-particle sizes, which constituted the plume, each had the same background spatial distribution. In this nonlinear study, each SMD particle size independently evolves in space and time. To ease interpretation of the SMD-modified evolution of the AEWs, we use the analytical expression derived by Grogan et al. (2016) for the local generation/destruction of eddy APE by the direct radiative effects of SMD (denoted by $\overline{\mathrm{GE}}_a$).

The expression for $\overline{\mathrm{GE}}_a$ is derived by combining the linearized thermodynamic and dust continuity equations, subsequently making three assumptions for the analytical analysis: the SMD heating rate is due solely to shortwave absorption, the sedimentation rate is a linear function of the SMD, and the perturbations (eddies) are normal mode in form. Together these assumptions yield

$$\overline{\mathrm{GE}}_a(y,p,t) = \underbrace{-C\left(A\overline{\gamma}_y + \frac{pf}{R}\frac{\partial \overline{u}}{\partial p}\frac{A}{\overline{S}}\overline{\gamma}_p\right)(\sigma_i\cos\phi + \sigma_r\sin\phi)|v||T|}_{\mathrm{I}} \underbrace{-\, C(\sigma_i k c_i + \sigma_r^2)\frac{A}{\overline{S}}\overline{\gamma}_p|T|^2}_{\mathrm{II}}, \qquad (3.1)$$

where y is the meridional direction, p is pressure, t is time, ϕ is the phase angle between the temperature (T) and meridional velocity (υ) fields, and

$$C = \frac{1}{2c_p\overline{S}(\sigma_r^2 + \sigma_i^2)}\exp(2kc_i t), \tag{3.2}$$

$$\sigma_i = kc_i - \frac{1}{c_p}\frac{A}{\overline{S}}\overline{\gamma}_p + D, \quad \text{and} \tag{3.3a}$$

$$\sigma_r = k(\overline{u} - c_r). \tag{3.3b}$$

In (3.1)–(3.3), the overbar denotes a zonal average; $\overline{u}(y, p, t)$ and $\overline{\gamma}(y, p, t)$ are the zonally averaged zonal wind and SMD mass mixing ratio; $c = c_r + ic_i$ is the complex phase speed; $A(y, p; \overline{\gamma})$ is a positive function that depends on the SMD transmissivity; $D(y, p)$ is the sedimentation rate, which is different for each of the 12 particle sizes; $f(y)$ is the Coriolis parameter; R is the gas constant for dry air; c_p is the specific heat capacity at constant pressure; and $\overline{S}(y, p) = -\overline{T}\,\overline{\theta}^{-1}\partial\overline{\theta}/\partial p$ is the static stability, where $\overline{\theta}(y, p)$ is the potential temperature.

Equation (3.1) shows that $\overline{\mathrm{GE}}_a$ depends on SMD-modified baroclinic effects (term I) and SMD-modified eddy APE (term II). Term I is controlled by $A\overline{\gamma}_y$ and $A\overline{\gamma}_p$, which are modulated by the Doppler-shifted frequency σ_r, the SMD-modified growth rate σ_i, and the phase angle between the meridional wind and temperature fields ϕ. Depending on the meridional and vertical gradients of the zonally averaged SMD distributions, $A\overline{\gamma}_y$ and $A\overline{\gamma}_p$ may augment or oppose each other. In contrast to the SMD-modified baroclinic term I, the SMD-modified eddy APE term II is independent of ϕ and controlled solely by $A\overline{\gamma}_p$. Thus term II in (3.1) decreases the eddy APE when the SMD decreases with height.

To facilitate the interpretation of the numerical results to be presented in section 4a, we make two further simplifications to (3.1). First, based on observations over West Africa (Reed et al. 1988), $\phi \approx 180°$ ($\cos\phi \approx -1; \sin\phi \approx 0$) below the AEJ and $\phi \approx 0°$ ($\cos\phi \approx 1; \sin\phi \approx 0$) above the AEJ. Second, our numerical integrations show that $A\overline{\gamma}_y$ generally dominates over $A\overline{\gamma}_p$ in term I, so we neglect the latter. With the two simplifications, (3.1) becomes

$$\overline{\mathrm{GE}}_a = F_1\hat{\overline{\gamma}}_y + F_2\hat{\overline{\gamma}}_p, \tag{3.4}$$

where

$$\hat{\overline{\gamma}}_y = -\delta\overline{\gamma}_y|\upsilon||T| \quad \text{and} \tag{3.5a}$$

$$\hat{\overline{\gamma}}_p = -\overline{\gamma}_p|T|^2. \tag{3.5b}$$

In (3.4), $F_1 = CA\sigma_i$ and $F_2 = C(\sigma_i kc_i + \sigma_r^2)A\overline{S}^{-1}$ are both positive during the growth stages of the AEW life cycle. In (3.5a), δ accounts for the phasing between the temperature and meridional wind fields: below the AEJ $\delta = -1$, whereas above the AEJ $\delta = +1$.

4. Numerical results

a. AEW life cycle

Thorncroft and Hoskins (1994b) and Thorncroft (1995) used an idealized primitive equation model without SMD to examine the nonlinear evolution of AEWs. They found that the nonlinear evolution of the eddy kinetic energy (EKE) is characterized by four stages: (i) initial linear growth dominated by barotropic energy conversions (CK), (ii) slowed but continued growth at finite amplitude due mostly to baroclinic conversions (CE), (iii) peak EKE and stabilization of the AEJ, and (iv) combined barotropic (CK) and baroclinic (CE) decay.

The nonlinear evolution of the domain-averaged (global) energetics, which were calculated following Norquist et al. (1977), are shown in Fig. 3 without SMD (NODUST) and with SMD (DUST). Consistent with Thorncroft and Hoskins (1994b), NODUST shows that the maximum EKE is ~40 × 10^3 J m^{-2} and that CK peaks before CE during stage II [cf. Fig. 1 in Thorncroft and Hoskins (1994b) with our Fig. 3a]. As discussed in Thorncroft and Hoskins (1994b), the timing of the peak in CE during stage II is due to the downward propagation of wave activity below the AEJ. In contrast to Thorncroft and Hoskins (1994b), NODUST shows that peak EKE occurs ~2 days earlier, peak CK is ~37.5% stronger, and peak CE is ~50% weaker. The differences between our results and those of Thorncroft and Hoskins (1994b) may not be surprising given the differences in the initial background fields, model resolutions, and numerical methods. For example, when our vertical resolution is chosen similar to Thorncroft and Hoskins (1994b), the timing and strength of our peak energy conversions differ from theirs by <10%. Most importantly, however, irrespective of our model resolution, the SMD influence on the life cycle of the modeled AEJ–AEW system is robust.

The domain-averaged energetics for NODUST and DUST show three differences. First, the SMD increases CK by as much as 65%, Fig. 3b, and CE by as much as 30%, Fig. 3c, during stages I and II (0–5 and 5–9 days)—that is, when the AEW is amplifying. Second, the SMD causes the peak EKE to occur ~1.5 days earlier and increase its maximum amplitude by ~25% during stage III (9–12 days); the earlier peak in EKE (~1.5 days) is due to the earlier peaks in CK and CE (~0.5 day each). Third, the SMD increases the barotropic and baroclinic decay rates by ~25%–100% during stage IV (12–20 days)—the final stage in the AEW life cycle.

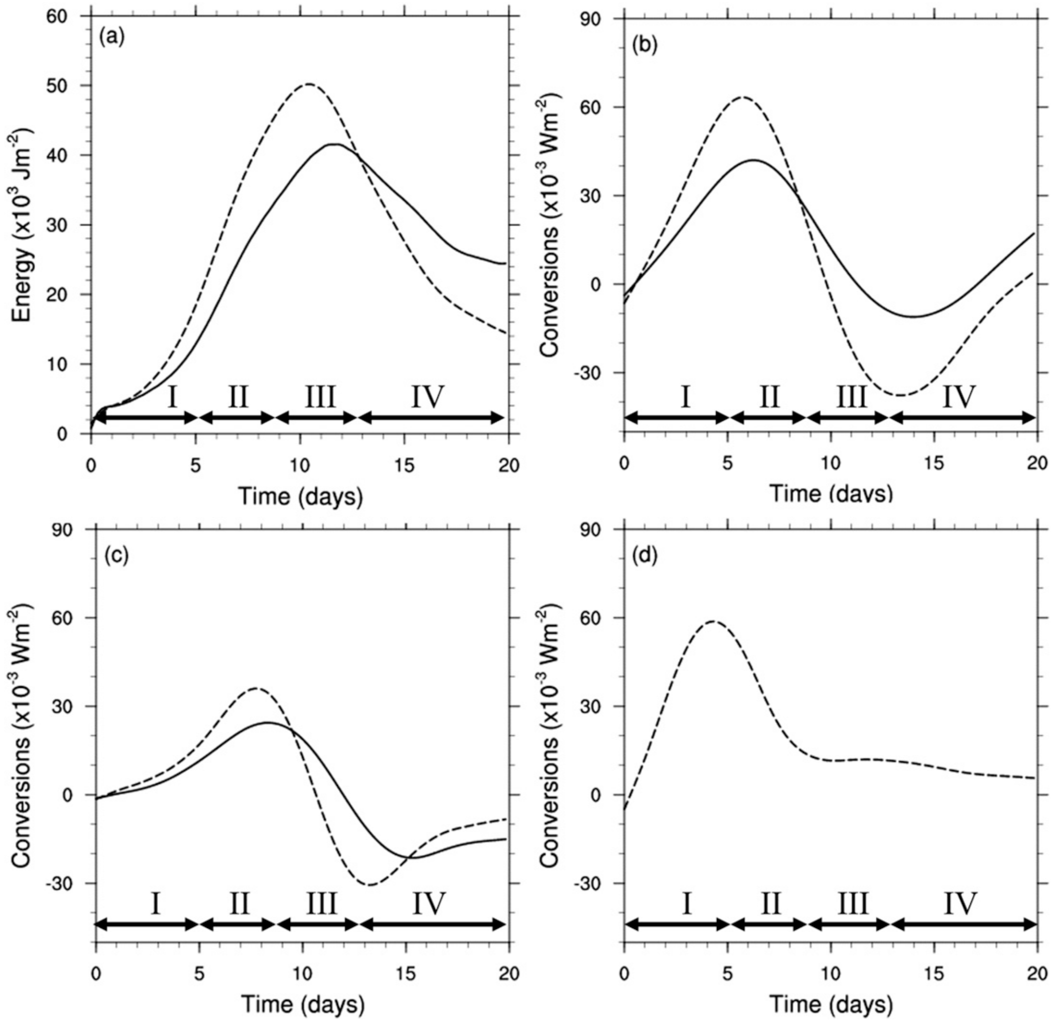

FIG. 3. Time evolution of domain-averaged energetics for the NODUST (solid) and DUST (dashed) experiments. (a) Domain-averaged EKE, (b) CK, (c) CE, and (d) GE. The double arrows denote the approximate duration of each of the four stages of the AEW life cycle.

Compared to the SMD-free AEW, the SMD-modified AEW reaches finite amplitude earlier and with greater energy and then decays at a faster rate.

The domain-averaged generation of eddy APE by the SMD field (GE) is shown in Fig. 3d. The figure shows that GE increases during stage I, peaking on day ~4, and then decreases during stage II, followed by continued but much slower decrease during stages III and IV.

To understand the evolution of GE, we consider its local generation, denoted by $\overline{\mathrm{GE}}$. Figure 4 shows $\overline{\mathrm{GE}}$ on days 4 and 7, which fall, respectively, within stages I and II of the AEW life cycle. Figure 4a shows that on day 4 of stage I, $\overline{\mathrm{GE}} > 0$ dominates a large region on the south side of the SMD plume (~15°–20°N). The location and structure of the generation region is consistent with the linear results obtained by Grogan et al. (2016): $\overline{\mathrm{GE}}$ is maximized at ~17°N between ~750 and 850 hPa. In this region, the maximum in $\overline{\gamma}_y$ is nearly coincident with the critical surface (thick curve in Fig. 4). Near the critical surface, $\overline{\gamma}_y > 0$, which, as described in section 3, generates eddy APE. Near the top of the SMD plume (~600 hPa), there is a small region where $\overline{\mathrm{GE}} < 0$. In this region, $\overline{\gamma}_p > 0$ and locally large, which, as described in section 3, destroys eddy APE.

In contrast to stage I (linear growth), $\overline{\mathrm{GE}}$ has a more complex structure during stage II (nonlinear stabilization). This is shown for day 7 in Fig. 4b. There are two regions of $\overline{\mathrm{GE}} > 0$, both at midlevel (~700 hPa) and on either side of the SMD plume (~10°–15° and ~20°–25°N). Within the SMD plume (~10°–20°N), there are also two regions where $\overline{\mathrm{GE}} < 0$: one at lower levels (~900–750 hPa) and the other at upper levels (~650–500 hPa). Like

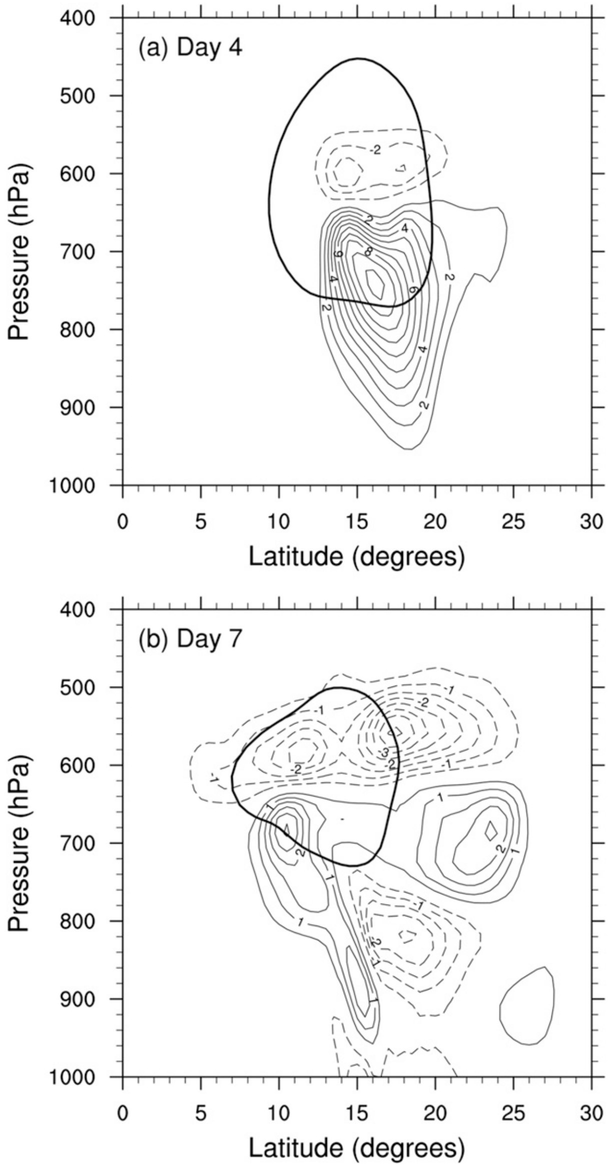

FIG. 4. $\overline{\mathrm{GE}}$ for (a) the linear growth stage and (b) the nonlinear stabilization stage of the AEW in the DUST experiment. Contour interval is $1.0 \times 10^{-7}\,\mathrm{m^2\,s^{-3}}$. Solid (dotted) contours indicate SMD generation (destruction) of eddy APE. The thick solid line denotes the critical surface.

the linear stage, Fig. 4b shows that the maximum generation in $\overline{\mathrm{GE}}$ is coincident with the critical surface (~11°N and ~700 hPa) and is large on the south side of the plume. But unlike the linear stage, this generation region is south of the AEJ axis (~13.5°N), and the generation regions on day 7 are, on average, ~80% weaker than the generation region on day 4. Moreover, Fig. 4b shows greater destruction of $\overline{\mathrm{GE}}$ at lower and upper levels, consistent with the decrease of GE shown in Fig. 3d.

We next examine the structural aspects of the eddy fields. A comprehensive analysis of the structural evolution of the eddy fields, however, is beyond the scope of this study. We therefore limit our discussion to the structural evolution of the 700-hPa (midlevel) perturbation meridional wind and 700-hPa SMD fields for selected days during each of the four stages of the AEW life cycle. We first note that the horizontal tilt of the perturbation shown in Fig. 5 is associated with barotropic energy conversions [section 7.3 of Pedlosky (1987)]. Consistent with Fig. 3b, Fig. 5 shows that the tilt of the AEW trough (thick line) for NODUST and DUST are associated with barotropic growth during stages I and II (Figs. 5a–d), weak barotropic energy conversions during stage III (Figs. 5e,f), and barotropic decay during stage IV (Figs. 5g,h). Figure 5 also shows that the wave structures for the two experiments are similar during their life cycle, but DUST has stronger meridional winds during stages I–III and weaker meridional winds during stage IV, which is consistent with the wave amplitude evolution shown in Fig. 3a.

The structural evolution of the midlevel SMD field shows several interesting features. For example, Fig. 5b shows that during stage I, the SMD rotates anticyclonically within the northerlies, which transport the SMD southward ahead (west) of the AEW trough. Such anticyclonic SMD transport is frequently observed for plumes that migrate from North Africa to the eastern Atlantic Ocean (Westphal et al. 1988; Karyampudi et al. 1999). The northerlies remain weak during stage I; consequently, the large concentrations remain near the SMD source region (18°–22°N). During stages II and III, Figs. 5d and 5f show that the midlevel SMD field continues to wrap up in the northerlies west of the trough. The enhanced northerlies during these stages transport large amounts of the midlevel SMD south of the AEJ, but the SMD mixing ratios are less than during stage I. The lesser mixing ratios are due to the coarser particles settling to the surface while the finer particles disperse and remain suspended in the atmosphere. As shown in Fig. 5h, during stage IV, the removal and smoothing of the SMD field continues, with few regions having SMD mixing ratios that exceed $50\,\mu\mathrm{g\,kg^{-1}}$.

b. *Evolution of the SMD plume*

Figure 6 shows the zonally averaged distribution of the SMD plume for the same representative stage days used in Fig. 5. During the linear growth (stage I), the structure of the SMD plume shown in Fig. 6a resembles the initial plume shown in Fig. 2. The largest concentrations are confined between ~18° and 22°N, with strong meridional SMD gradients on either side. The

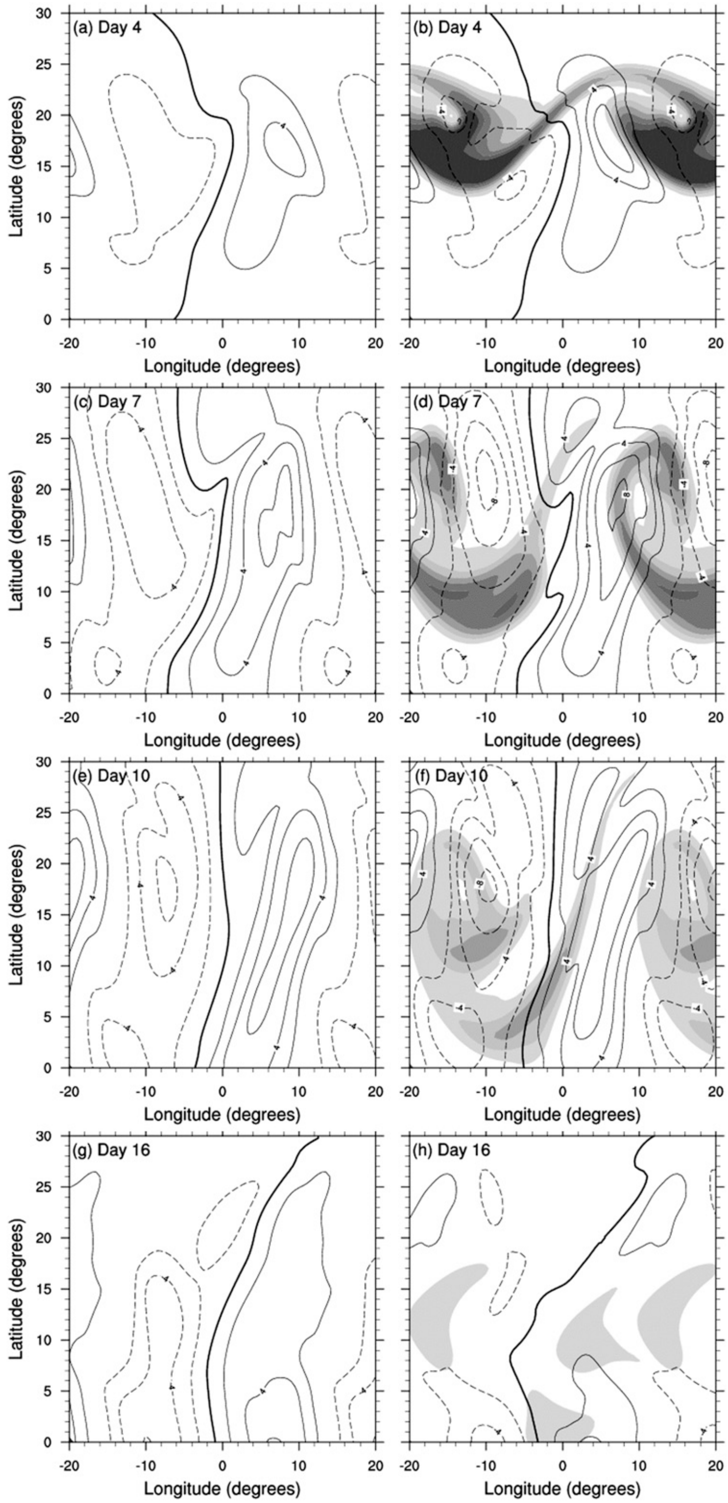

FIG. 5. Plots of the 700-hPa perturbation meridional wind (contours; m s^{-1}) for (a),(b) day 4 of stage I, (c),(d) day 7 of stage II, (e),(f) day 10 of stage III, and (g),(h) day 16 of stage IV for (left) NODUST and (right) DUST. The shading denotes the 700-hPa SMD mixing ratio (μg kg^{-1}). Contour intervals are 2 m s^{-1} for the meridional wind and 50.0 μg kg^{-1} for the SMD mixing ratio; the darkest shade corresponds to 300 μg kg^{-1}. Also shown is the AEJ trough at 700 hPa (thick solid line).

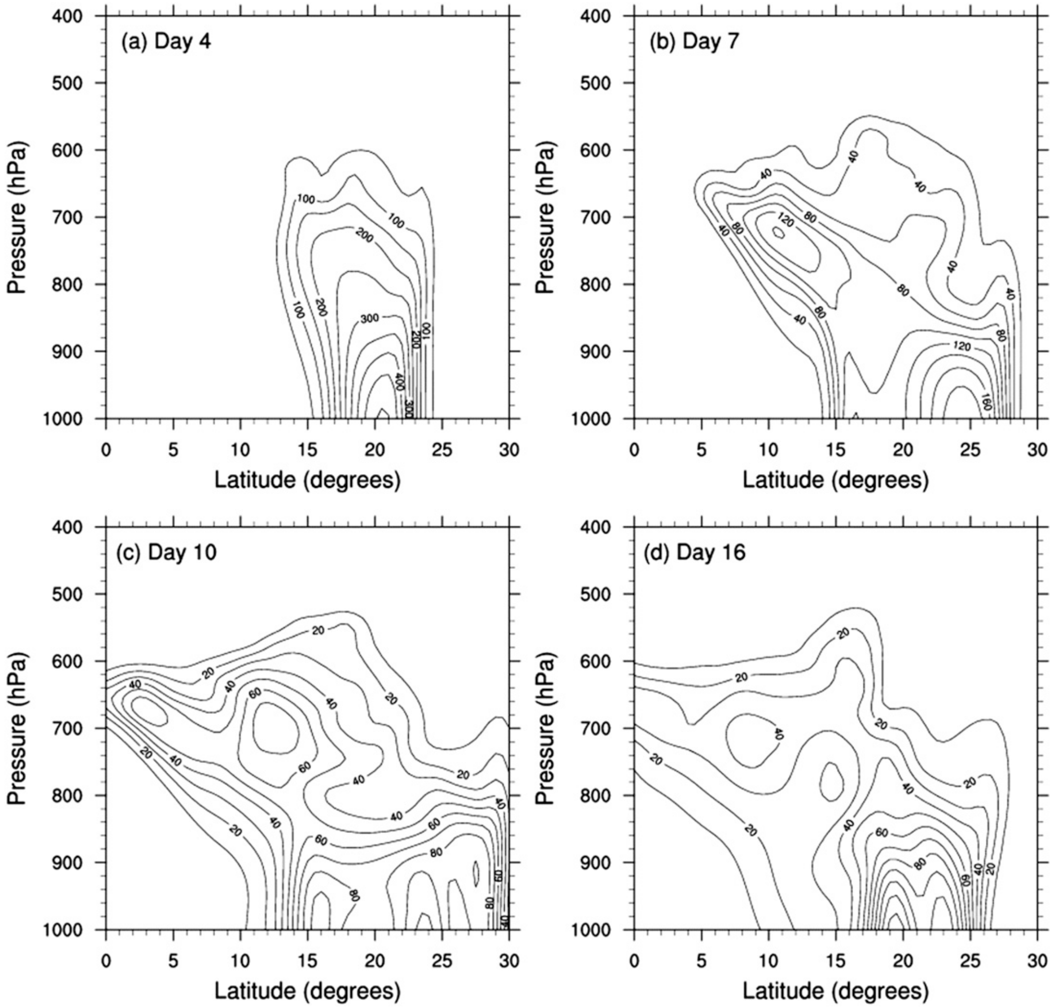

FIG. 6. Zonally averaged distributions of the total SMD mixing ratio for the same days as in Fig. 5. Contour intervals are (a) 50.0, (b) 20, and (c),(d) 10 μg kg^{-1}.

strong gradients are essential to the generation of $\overline{\mathrm{GE}}$, as shown analytically in section 3. Moreover, the regions of large meridional SMD gradients coincide with the regions of large SMD-modified energetics (Grogan et al. 2016). Although the zonally averaged structure of the plume does not change much during the linear growth stage, the total SMD concentration does; it diminishes as a result of gravitational settling, mostly by the coarser SMD particles. The total SMD mixing ratio decreases from its initial maximum of ~800 to ~500 μg kg^{-1} on day 4, a reduction of ~37.5%. The three coarsest SMD particles (radius $> 1\,\mu$m) are ~50% of their initial concentrations, whereas the three finest SMD particles (radius $< 0.25\,\mu$m) are ~99% of their initial concentrations.

Figure 6b shows that during nonlinear stabilization (stage II) the SMD is transported southward at midlevels and northward at low levels. Consequently, there are local maxima at ~11°N and ~730 hPa and ~25°N and ~1000 hPa. The transport also widens the plume by ~10° at midlevels, and by ~4° at the base. Recall, the southward transport at midlevels, which was shown in Fig. 5, is due to enhanced northerlies that rotate the SMD anticyclonically ahead of the trough. Structural changes in the SMD plume are also due to the separation of SMD particles sizes: finer particles that remain suspended continue to expand southward toward the AEJ (~700 hPa), while the coarser particles settle to the surface more efficiently away from the AEJ. The discrimination between SMD particles is seen in Fig. 7, which shows the zonally averaged distributions of the model's coarsest and finest SMD particles. The coarsest particle distribution (Fig. 7a) is meridionally asymmetric and is mostly concentrated

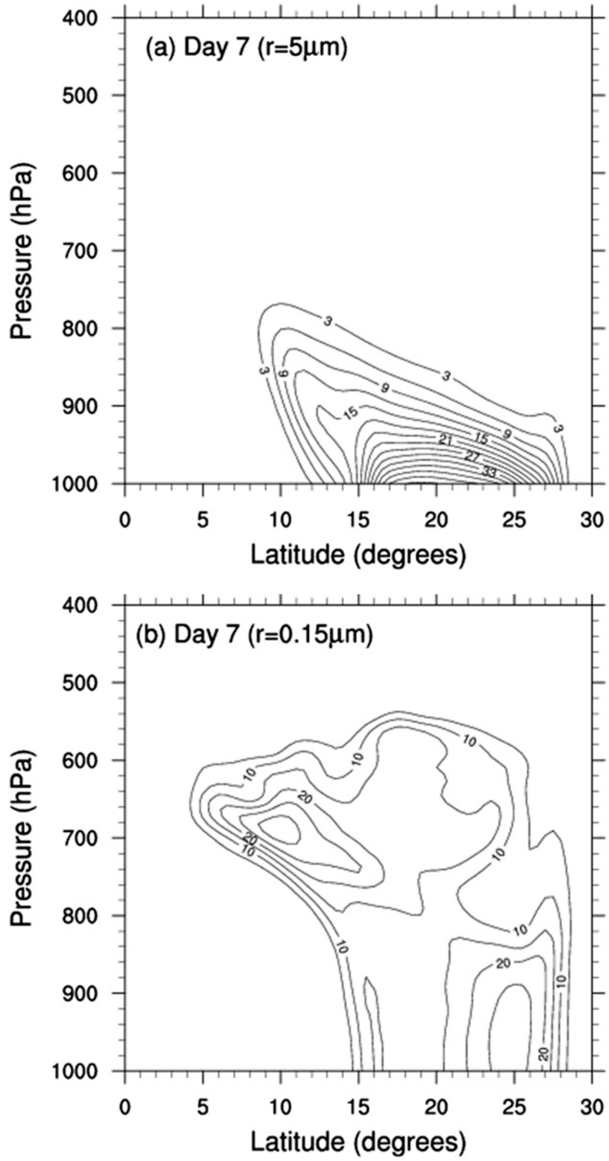

FIG. 7. SMD mixing ratios for (a) the coarsest and (b) the finest particles on day 7. The particle radius is shown in each figure. Contour intervals are (a) 3.0×10^{-3} and (b) $5.0 \times 10^{-3}\,\mu\mathrm{g\,kg^{-1}}$.

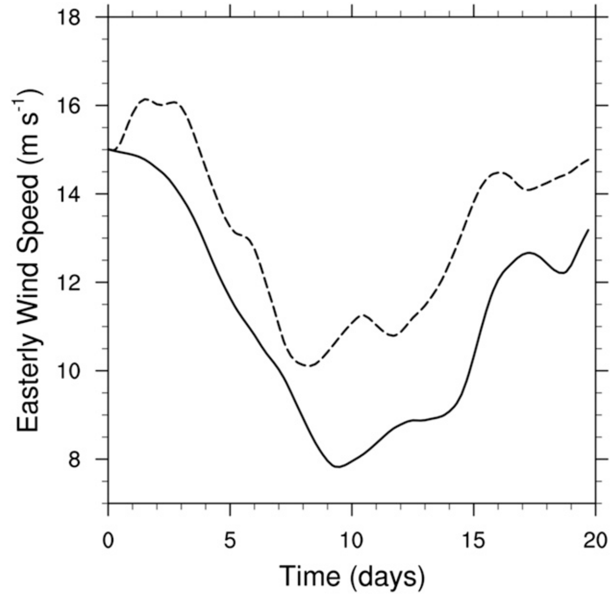

FIG. 8. Peak zonally averaged zonal wind speeds for the NODUST (solid) and DUST (dashed) experiments.

near the surface, such that $\overline{\gamma}_p > 0$ everywhere. The finest SMD particle distribution (Fig. 7b) resembles the total SMD distribution shown in Fig. 6b, which is characterized by several regions where $\overline{\gamma}_p$ and $\overline{\gamma}_y$ reverse sign. These sign reversals have implications for the generation and destruction of $\overline{\mathrm{GE}}$, which we discuss later in section 5b.

During peak amplitude and decay (stages III and IV), the SMD plume continues to expand vertically and meridionally, owing mostly to the transport of the finer SMD particles. Figures 6c and 6d show that the overall concentration of the zonally averaged plume shows little change between stages III and IV. For example, the maximum SMD mixing ratios on days 10 and 16 are $\sim$100 $\mu\mathrm{g\,kg^{-1}}$ near the surface, which is $\sim$12.5% of its initial value. During these stages, the SMD gradients are much weaker, which, as shown in Fig. 3d, corresponds to much weaker GE.

c. Evolution of the AEJ

Figure 8 shows the evolution of the peak zonally averaged wind speed for the NODUST and DUST experiments. During the first 10 days of NODUST, the peak wind speed monotonically decelerates at the rate of $\sim$1.0 m s^{-1} day^{-1} for days 3–8. For DUST, however, the peak wind speed accelerates during the first 2 days and then decelerates at the rate of $\sim$1.2 m s^{-1} day^{-1} for days 3–7, reaching its weakest speed on day 8, which is about a day earlier than NODUST. During days 10–20, NODUST and DUST show an oscillatory rebuilding of the peak wind speed, though the SMD-modified wind remains $\sim$1–2 m s^{-1} ($\sim$20%) stronger than the SMD-free wind.

To understand the SMD-induced changes to the zonally averaged zonal wind, we use the transformed Eulerian-mean (TEM) framework (Andrews and McIntyre 1976; Holton 2004). In this framework the equation for the zonally averaged wind $\overline{u}$ can be written as

$$\frac{\partial \overline{u}}{\partial t} = f\overline{v}^{\,*} + \nabla \cdot \mathbf{F} + \overline{X}. \qquad (4.1)$$

In (4.1) $\overline{v}^*$ is the residual meridional velocity; it is determined from the residual streamfunction, which depends on the divergence of EP flux, $\nabla\cdot\mathbf{F}$, as well as the northward gradient of the zonally averaged diabatic heating rate $\overline{Q}_y$ (e.g., Holton 2004); $\overline{X}$ is the zonally averaged mechanical damping, which is weak in our model and thus will not be considered further.

Figures 9a and 9b show the time evolution of $f\overline{v}^*$ and $\nabla\cdot\mathbf{F}$ at the location of the peak winds during the AEW life cycle. Because the zonally averaged flow is easterly, local accelerations occur when $\overline{v}^* < 0$ and $\nabla\cdot\mathbf{F} < 0$; decelerations occur otherwise. A comparison of Figs. 9a and 9b shows that $f\overline{v}^*$ and $\nabla\cdot\mathbf{F}$ oppose each other from stage I to near the end of stage IV. The opposition of these two fields, as explained by Trenberth (1986), ensures that thermal wind balance is maintained. During the first 10 days of the experiments, the easterly flow is accelerated by $\overline{v}^*$ and decelerated by $\nabla\cdot\mathbf{F}$; the opposite is true for the latter 10 days.

Figure 9 shows that the SMD generally strengthens $f\overline{v}^*$ and $\nabla\cdot\mathbf{F}$. During the first 2 days of the evolution, the SMD strengthens $f\overline{v}^*$, which dominates over $\nabla\cdot\mathbf{F}$, resulting in an acceleration of the peak wind speed. The SMD-enhanced $f\overline{v}^* < 0$ arises from the initially imposed SMD field, which causes the zonally averaged SMD heating rate to increase with latitude at the AEJ axis; that is, $\overline{Q}_y > 0$ dominates over $\nabla\cdot\mathbf{F}$ in the residual circulation equation such that $\overline{v}^* \propto -\overline{Q}_y$ (Holton 2004). During about days 3–7, $\nabla\cdot\mathbf{F}$ dominates over $f\overline{v}^*$ for both NODUST and DUST, which causes the peak wind speed to decelerate. The deceleration is faster for DUST than NODUST, a consequence of the SMD-modified $\nabla\cdot\mathbf{F}$ being ~30% larger, despite some offset by the SMD-modified $f\overline{v}^* < 0$. Around day 8, the peak wind speed reaches its local minimum of ~10 m s^{-1} in DUST, shown in Fig. 8, which occurs ~1 day earlier than the local minimum of ~8 m s^{-1} in NODUST. After ~day 10, $f\overline{v}^*$ and $\nabla\cdot\mathbf{F}$ reverse roles. At this time, the effects of SMD are diminished as a result of a reduction in its concentration and a smoothing of its spatial gradients (see section 4b). The reacceleration of the peak wind exhibits a similar pattern for NODUST and DUST.

Figures 10–13 show the connection between the AEJ and the EP cross sections for NODUST and DUST during each stage of the AEW life cycle. The top panels of Figs. 10–13 show the EP flux vectors $\mathbf{F}$, which approximate the direction of propagation of wave activity,[2]

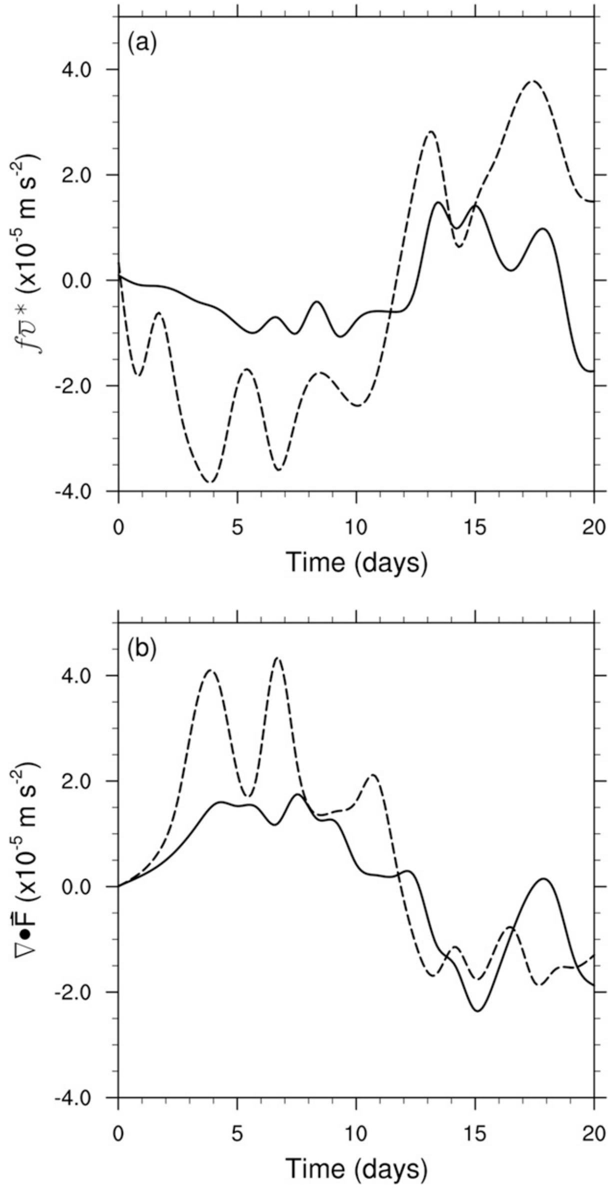

FIG. 9. Time evolution of (a) $f\overline{v}^*$ and (b) $\nabla\cdot\mathbf{F}$, calculated at the location of the peak zonally averaged wind for the NODUST (solid) and DUST (dashed) experiments. Because the zonally averaged wind evolves during the simulation, the quantities in (a) and (b) were computed at the location of peak wind for each time step.

and the EP flux divergence $\nabla\cdot\mathbf{F}$, which is a measure of the wave driving of the zonally averaged flow shown in (4.1). The bottom panels show the zonally averaged wind and its axis, which is located at the peak in easterly wind.

During linear growth (stage I), Figs. 10a and 10b show, as expected, that the structure of $\nabla\cdot\mathbf{F}$ agrees with the structure obtained in the linear study of Grogan et al. (2016). For NODUST and DUST, the pattern of $\mathbf{F}$ indicates propagation of wave activity away from the AEJ;

[2] In a slowly varying, zonally averaged background flow, the EP flux vectors are locally parallel to the group velocity and are therefore locally parallel to the propagation of wave activity (Edmon et al. 1980).

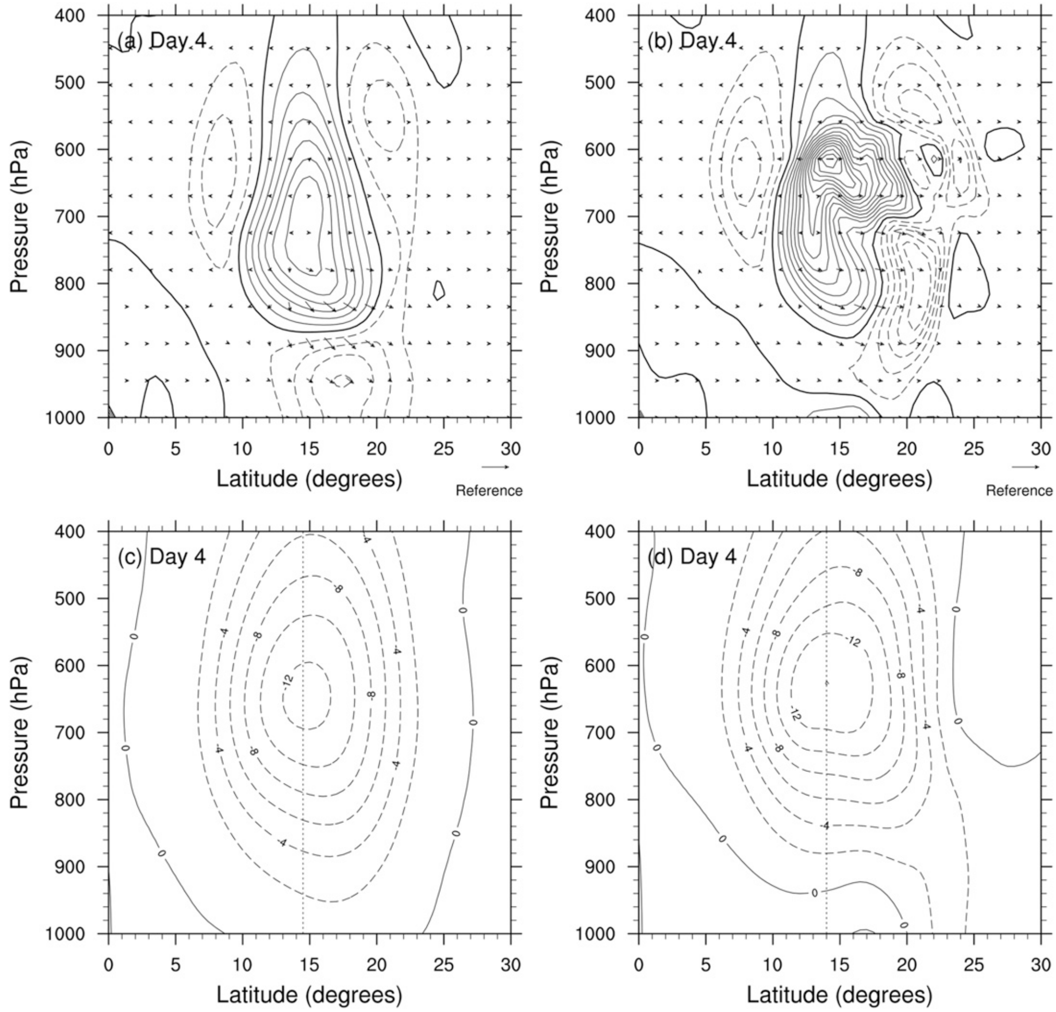

FIG. 10. (a),(b) EP flux vectors (**F**; arrows) and their divergence ($\nabla \cdot \mathbf{F}$; contours). (c),(d) Zonally averaged wind for the (left) NODUST and (right) DUST experiments during linear growth (stage I; day 4). Solid contours are positive, and dashed contours are negative. The EP flux vectors in (a) and (b) are scaled up in the figure; the reference vectors outside the plot measure 1×10^{13} m^3 for the horizontal component of **F** and 2×10^{17} m^3 Pa for its vertical component. Contour intervals are (a),(b) 5×10^{14} m^3 and (c),(d) 2 m s^{-1}. The vertical dotted line in (c) and (d) denotes the AEJ axis.

$\nabla \cdot \mathbf{F} > 0$ in the region surrounding the AEJ, with $\nabla \cdot \mathbf{F} < 0$ in the two flanking regions. This $\nabla \cdot \mathbf{F}$ pattern corresponds to reduction in the horizontal and vertical shear of the AEJ (cf. Fig. 1 with Figs. 10c,d). The $\nabla \cdot \mathbf{F}$ pattern, which is stronger for DUST than NODUST, has a secondary lobe of $\nabla \cdot \mathbf{F} < 0$ on the poleward flank of the AEJ axis (20°N and ~750–900 hPa). This lobe is a manifestation of the strong, positive meridional SMD gradients between the AEJ axis (~15°N) and the SMD concentration axis (~20°N). In this region, the SMD-enhanced $\nabla \cdot \mathbf{F}$ pattern is due to enhanced momentum fluxes associated with increased barotropic growth (Fig. 3b). Consequently, this SMD-enhanced wave driving on the poleward flank of the AEJ more efficiently decelerates the flow there, which elevates the AEJ by ~50 hPa and shifts the AEJ axis ~0.5° south of its SMD-free location (Fig. 10c, dotted line).

During nonlinear stabilization (stage II), the $\nabla \cdot \mathbf{F}$ pattern for NODUST and DUST (Figs. 11a and 11b) corresponds to continued shear reduction of the AEJ (Figs. 11c and 11d). Compared to the linear growth stage, both experiments show expansion of $\nabla \cdot \mathbf{F} > 0$ surrounding the AEJ and stronger $\nabla \cdot \mathbf{F} < 0$ at mid-levels on its equatorward flank (~3°–8°N) and at low levels on its poleward flank (~16°–20°N). The stronger $\nabla \cdot \mathbf{F} < 0$ is associated with enhanced **F**, corresponding to the parallel tracks of wave activity on either side of the AEJ (Thorncroft and Hodges 2001). The tracks are

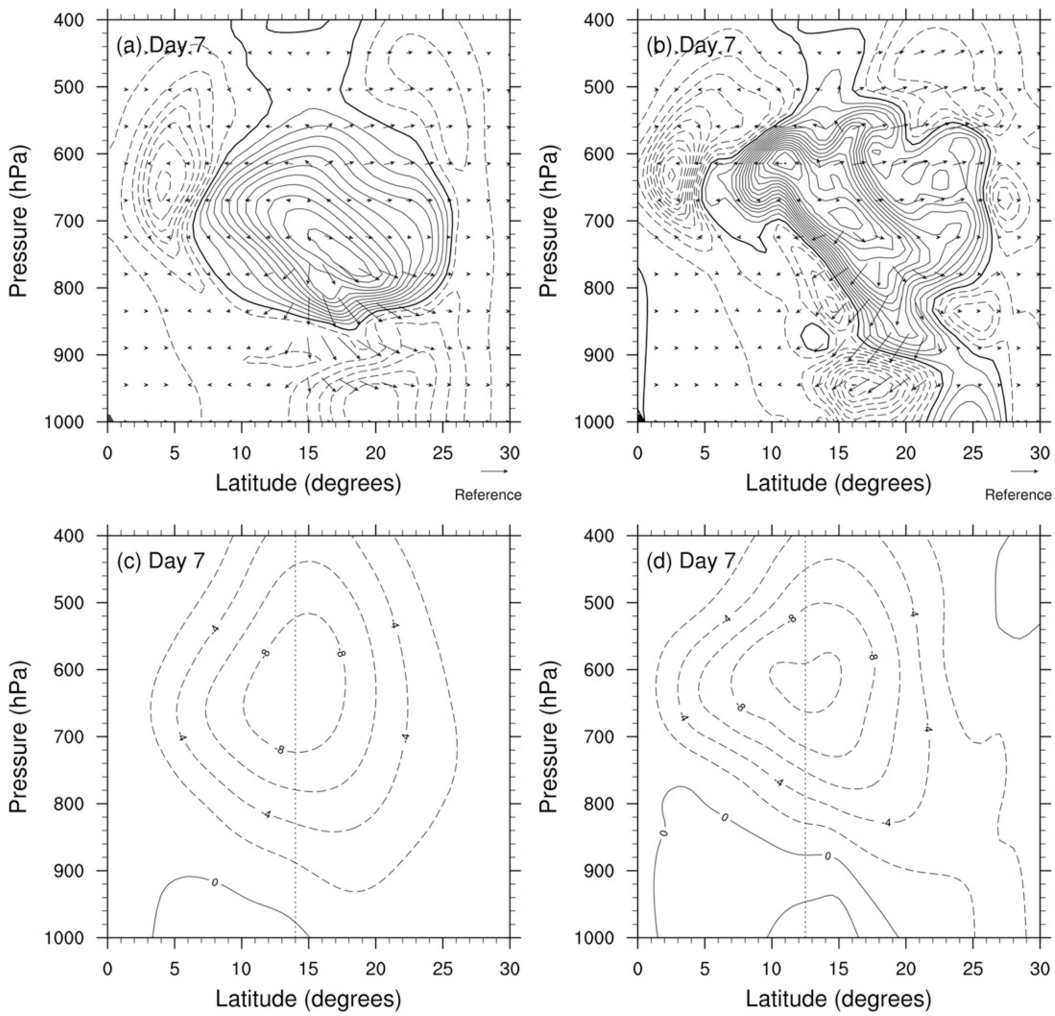

FIG. 11. As in Fig. 10, but during the nonlinear stabilization of the AEW (stage II; day 7).

primarily due to increased momentum fluxes (barotropic energy conversions), but increased heat fluxes (baroclinic energy conversions) are also important on the poleward flank. In contrast to the NODUST experiment, the DUST experiment shows that $\nabla \cdot \mathbf{F}$ is spatially asymmetric and more complex. For example, Fig. 11b shows that the $\nabla \cdot \mathbf{F} > 0$ region sharply contracts below ~700 hPa and extends down to the surface, between 16° and 20°N, while the region of $\nabla \cdot \mathbf{F} < 0$ at the surface increases by 50% and shifts southward, below the AEJ axis. Consequently, these SMD-induced changes in the $\nabla \cdot \mathbf{F}$ structure produce stronger surface easterlies north of the AEJ, stronger surface westerlies below the AEJ, and stronger vertical shear between ~8° and 16°N and between 650 and 850 hPa (Fig. 11d). Meanwhile, like the linear growth stage, the SMD-modified AEJ axis remains south of its SMD-free location by ~1.5°.

Figure 12 shows that the peak amplitude during stage III is marked by a transition in the structure of $\nabla \cdot \mathbf{F}$ and its driving of the AEJ. In contrast to stages I and II, NODUST and DUST show that the EP flux vectors now point equatorward on the poleward flank of the AEJ (Figs. 12a and 12b), corresponding to barotropic energy decay, as in Thorncroft and Hoskins (1994b). The $\nabla \cdot \mathbf{F}$ pattern indicates rebuilding of the AEJ, whose axis is farther south of its stage I and stage II locations. Like stage II, however, the SMD-modified $\nabla \cdot \mathbf{F}$ shows a complex structure (see Fig. 12b); there are steeper gradients and multiple local maxima, with one located at the surface. Figure 12b shows, for example, that the SMD increases $\nabla \cdot \mathbf{F} < 0$ on the equatorward flank of the AEJ (between 3° and 5°N at 700 hPa) and increases $\nabla \cdot \mathbf{F} > 0$ on its poleward flank (between 10° and 15°N and 650 and 550 hPa). This $\nabla \cdot \mathbf{F}$ pattern affects the structure of the AEJ as it begins to rebuild—the SMD-enhanced

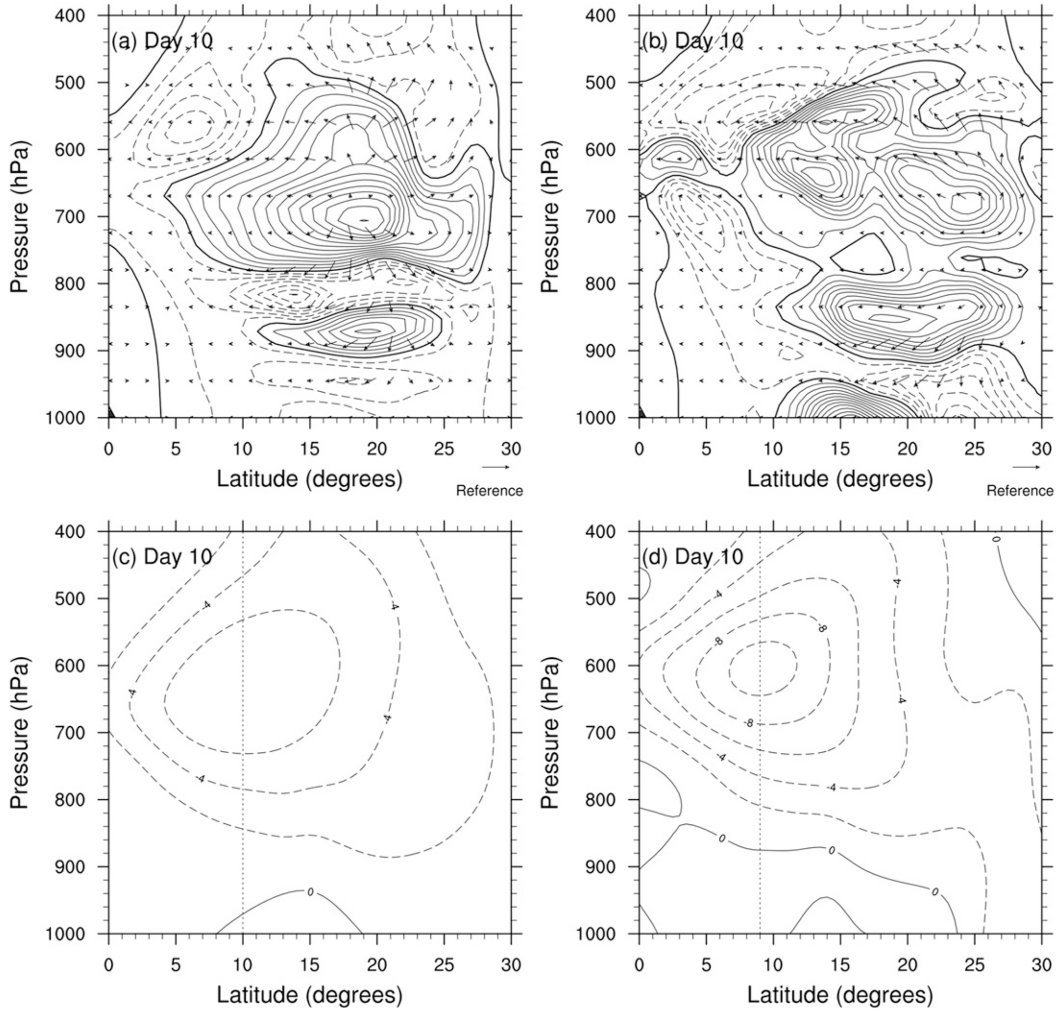

FIG. 12. As in Fig. 10, but during peak amplitude (stage III; day 10).

$\nabla \cdot \mathbf{F}$ pattern increases the horizontal shear on either side of the AEJ.

During stage IV (wave decay), the $\nabla \cdot \mathbf{F}$ pattern for NODUST and DUST (Figs. 13a and 13b) is consistent with the rebuilding of the AEJ due to baroclinic and barotropic decay of the AEW. For both experiments, the EP flux vectors point upward and equatorward from the surface to the AEJ. Moreover, the AEJ in DUST and NODUST are surrounded by a region of $\nabla \cdot \mathbf{F} < 0$ (10°N and 600 hPa) and weaker regions of $\nabla \cdot \mathbf{F} > 0$ at mid- (~650 hPa) and low (950 hPa) levels on the northern flank of the AEJ (15°–20°N). The region $\nabla \cdot \mathbf{F} < 0$ surrounding the AEJ is similar in magnitude for both experiments, but the maximum in NODUST (Fig. 13a) is south of the maximum in DUST (Fig. 13b). Because the location of the maximum in $\nabla \cdot \mathbf{F} < 0$ drives the strongest easterly flow, the AEJ axis shifts southward of its position in stage III. The SMD-induced shift, however, is less than the SMD-free case. Thus on day 16, the AEJ for NODUST and DUST are collocated (7°N in Figs. 13c and 13d). By day 20, the SMD-modified AEJ axis sits ~2° north of its SMD-free location.

d. Sensitivity to the initial AOD and plume location

The results presented in sections 4a–4c were obtained for an initial SMD plume that was chosen consistent with observations: maximum AOD (τ) = 1.0 centered at 20°N. Observations show, however, that $\tau > 1.0$ commonly occurs over the Sahara Desert (Tulet et al. 2008)—that is, near the major dust source regions, which are located between ~18° and 22°N (Engelstaedter and Washington 2007). In this subsection, we retain the initial structure of the plume used in sections 4a–4c, but change the maximum τ and its location in order to examine the effects on the AEW life cycle.

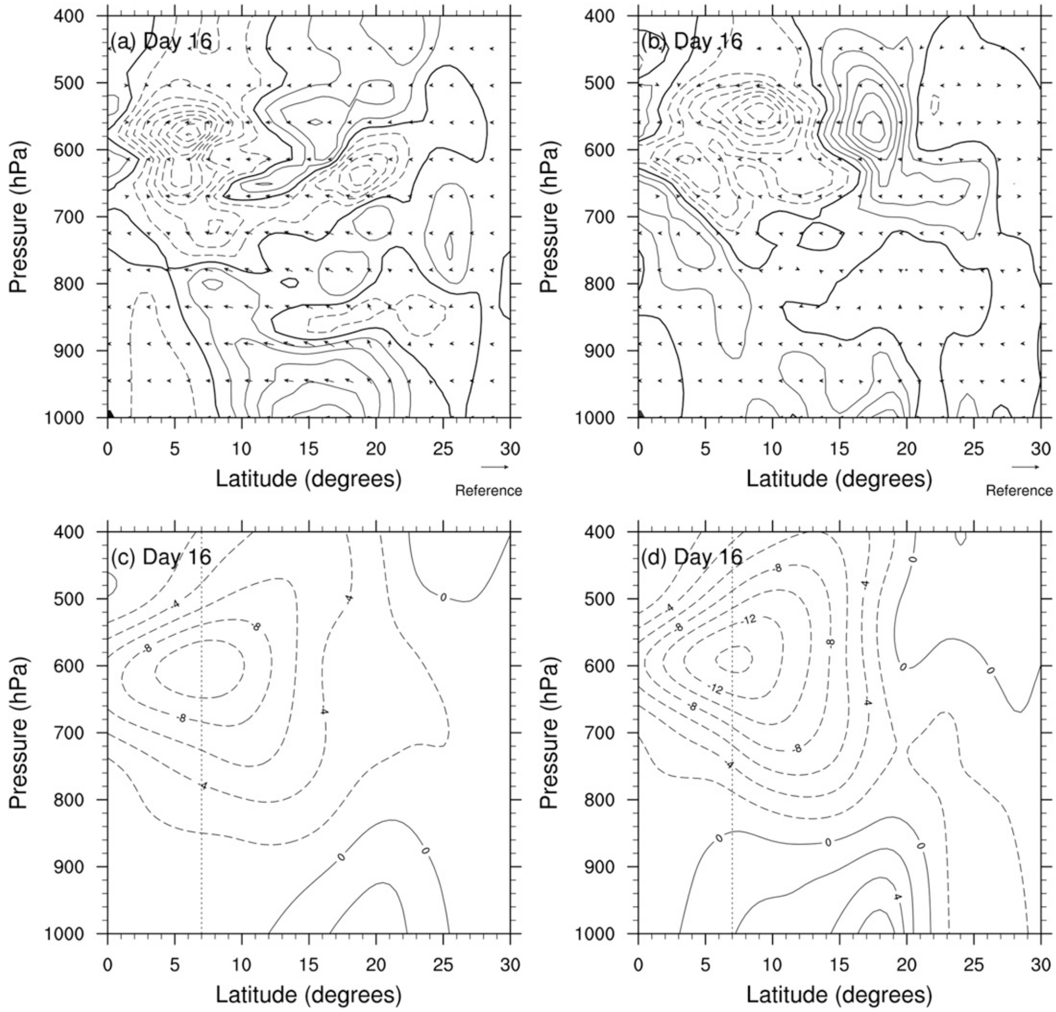

FIG. 13. As in Fig. 10, but during wave decay (stage IV; day 16).

Figure 14 shows that over the AEW life cycle, the domain-averaged EKE monotonically increases with increasing τ. For τ = 1.0, 2.0, and 3.0, the peak EKE is 11%, 20%, and 45% larger than NODUST, respectively. Figure 14 also shows that the timing of the peak EKE amplitude (stage III) is nonmonotonic; for τ =1.0, 2.0, and 3.0, the peak amplitudes occur at 10.5, 10, and 11 days, respectively.

Figure 15 shows the sensitivity of the domain-averaged EKE to changes in the location of τ. The figure shows that the plume location affects the peak amplitude (stage III) but not its timing. The EKE is maximized when the plume is centered at ~21°–22°N (Fig. 15; thin dotted–dashed); at this location, the maximum EKE is ~8% larger than at 20°N (Fig. 15; solid). This nonlinear result is in agreement with the linear result obtained by Grogan et al. (2016), who showed that the largest linear growth rates occurred for a plume centered at ~21°N. As the plume moves closer to the AEJ axis (15°N), the maximum EKE monotonically decreases.

5. Analysis

In this section, we delve more deeply into the SMD-modified radiative and dynamical interactions that govern the life cycle of the AEW. We begin with a model nonlinear equation that exposes how SMD affects each stage of the AEW life cycle. We then show how the distribution of different SMD particle sizes affects the local generation and destruction of eddy APE.

a. SMD-modified AEW life cycle

The results presented in the previous section show that over the life cycle of the AEW the SMD enhances the linear growth rate (stage I), reduces the nonlinear

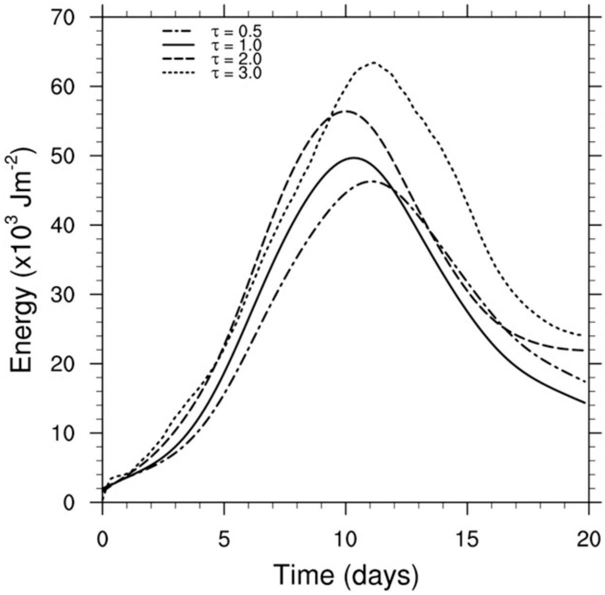

FIG. 14. The evolution of the domain-averaged EKE as a function of the maximum AOD (τ) for the SMD plume shown in Fig. 2: $\tau = 0.5$ (dotted–dashed), 1.0 (solid), 2.0 (dashed), and 3.0 (dotted).

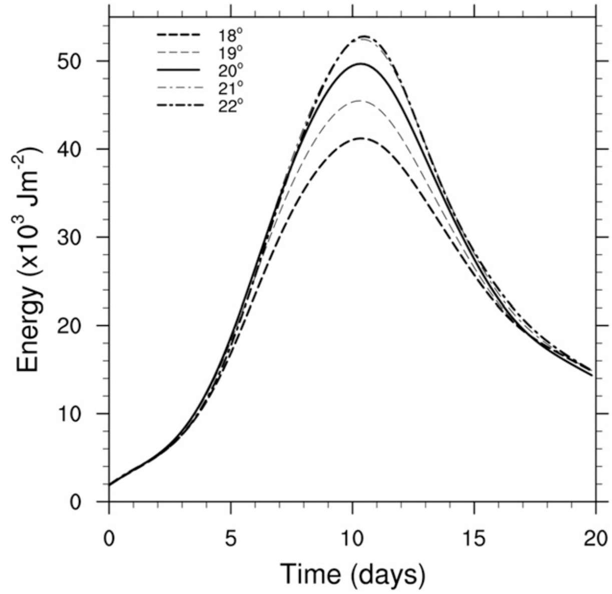

FIG. 15. The evolution of the domain-averaged EKE as a function of the central latitude for the SMD plume distribution shown in Fig. 2. Central latitudes are 18° (thick dash), 19° (thin dash), 20° (thick solid), 21° (thin dotted–dashed), and 22°N (thick dotted–dashed). For each case $\tau = 1$.

stabilizing effect (stage II), produces larger peak amplitude (stage III), and increases the decay rate (stage IV). To provide insights into the SMD-modified physics that governs the life cycle of the AEW, we examine the following model equation that describes the nonlinear evolution of a linearly unstable wave:

$$\frac{d^2\tilde{A}}{dt^2} + [-G^2 + N(|\tilde{A}_w|^2 - |\tilde{A}_0|^2)]\tilde{A} = 0, \qquad (5.1)$$

where $\tilde{A}$ is a complex amplitude, $\tilde{A}_0$ is the initial amplitude, and G and N are positive constants. Equations of the form of (5.1) arise in several geophysical fluid contexts, including the finite-amplitude dynamics of baroclinic waves in β- and f-plane geometries, in layered and stratified atmospheres, and in studies of temporally and spatially growing waves (Pedlosky 1970; Merkine 1978; Pedlosky 1987; Nathan 1993, 1998). As discussed by Pedlosky (1987), (5.1) describes a mass–spring oscillator where the "spring force" is repulsive for small amplitude and restoring for large amplitude. When the amplitude is small, the wave grows at the linear growth rate G (stage I). For sufficiently large amplitude, however, the spring force is restoring, which can be seen by writing the effective local growth rate as

$$\left(\frac{1}{\tilde{A}}\frac{d^2\tilde{A}}{dt^2}\right)^{1/2} = [G^2 - N(|\tilde{A}|^2 - |\tilde{A}_0|^2)]^{1/2}. \qquad (5.2)$$

Thus as the wave grows to finite amplitude, the effective growth rate is reduced (stage II), eventually vanishing when $\tilde{A}^2 = G^2N^{-1} + \tilde{A}_0^2 = 0$, which is also an equilibrium point of (5.1). But the wave will continue to grow beyond its equilibrium point because of inertia, though at an increasingly slower rate, eventually reaching its maximum amplitude (stage III):

$$\tilde{A}^2_{\max} = \tilde{A}_0^2 + \frac{G^2}{N} + \left[\left(\frac{G^2}{N}\right)^2 + 2\tilde{A}_0^2\right]^{1/2}. \qquad (5.3)$$

Equation (5.3) is obtained by multiplying (5.1) by $d\tilde{A}/dt$ to obtain a first integral, where $\tilde{A}$ is assumed real without loss of generality. Equation (5.3) shows that $\tilde{A}_{\max}$ increases as the linear growth rate G increases. When $\tilde{A}$ is maximized, the effective linear growth is also maximized but negative, such that the amplitude will diminish with time (stage IV). The amplitude will continue to diminish until the effective growth rate again becomes positive and the nonlinear cycle is repeated.

Equations (5.1)–(5.3) qualitatively explain how the direct radiative effects of SMD influence the AEW life cycle shown in Fig. 3a. During the linear growth phase (stage I), the SMD increases the growth rate, in agreement with the linear study of Grogan et al. (2016). As shown in (5.2), a larger linear growth rate requires larger wave amplitude before the effective growth rate vanishes and the wave begins to slow its growth. This is seen, for example, at day 7 in stage II, when the SMD-modified EKE is ~30% larger than without SMD. As predicted by (5.3), the SMD-enhanced linear growth rate results in larger wave amplitude and thus larger EKE (stage III). Consequently, the spring force is also larger, which causes the wave to decay more rapidly than it would without the SMD radiative feedbacks (stage IV).

b. Particle size distribution and local destruction of eddy APE

We have shown analytically in section 3 that the local generation/destruction of eddy APE by the SMD field depends on the meridional and vertical gradients of zonally averaged SMD, which are modulated by the Doppler-shifted frequency. In section 4a, we showed $\overline{\mathrm{GE}}$ for specific days during linear growth (stage I) and the nonlinear stabilization (stage II) of the AEW life cycle. In this subsection, we revisit stage II and examine the effects of the SMD particle size distribution on the destruction of $\overline{\mathrm{GE}}$, which occurs at lower levels (~900–800 hPa) and upper levels (~650–500 hPa) within the SMD plume (~10°–20°N) (see Fig. 4b).

Figure 16 shows $\hat{\overline{\gamma}}_{y,\bar{j}}$ and $\hat{\overline{\gamma}}_{p,\bar{j}}$ at day 7 of stage II; the subscript $\bar{j}$ represents the particle size ($\bar{j}=\bar{c}$ for the coarsest particle; $\bar{j}=\bar{f}$ for the finest particle). Recall, $\hat{\overline{\gamma}}_y \propto A\overline{\gamma}_y$ and $\hat{\overline{\gamma}}_p \propto A\overline{\gamma}_p$, which are defined by (3.5a) and (3.5b). For the coarsest particle (radius = 5 μm) in the region between ~15° and 20°N and between ~900 and 800 hPa, which is below and north of the AEJ axis, $\overline{\gamma}_y < 0$ and $\overline{\gamma}_p > 0$ (see Fig. 7a), and the eddy heat flux is negative such that $\delta = -1$ in (3.5a). Consequently, $\hat{\overline{\gamma}}_{y,\bar{c}}$ and $\hat{\overline{\gamma}}_{p,\bar{c}}$ combine to destroy eddy APE [see (3.4)]. At low levels, the spatial gradients of the coarse particles are larger than for the fine particles (cf. 700–900 hPa in Figs. 7a and 7b). Thus $\hat{\overline{\gamma}}_{y,\bar{c}}$ and $\hat{\overline{\gamma}}_{p,\bar{c}}$ are the main contributors to the low-level destruction of $\overline{\mathrm{GE}}$ shown in Fig. 4b.

Figures 16c and 16d show that relative to the course SMD particles, $\hat{\overline{\gamma}}_{y,\bar{f}}$ and $\hat{\overline{\gamma}}_{p,\bar{f}}$ have a more complex structure, evidenced by multiple generation and destruction regions of eddy APE. Although the fine SMD particles initially have the smallest mixing ratios, their spatial gradients remain large at the plume top (above 650 hPa). Figure 16c shows that at ~600 hPa and between ~10° and 20°N, $\hat{\overline{\gamma}}_{y,\bar{f}}$ has two alternating destruction and generation regions. In contrast, Fig. 16d shows that $\hat{\overline{\gamma}}_{p,\bar{f}}$ has two local destruction regions centered at ~11°N and ~600 hPa and at ~18°N and ~550 hPa. These destruction regions are associated with the largest spatial gradients of the fine SMD particles above 650 hPa. In this region, the zonally averaged distribution of the fine particles shown in Fig. 7b is such that $\overline{\gamma}_p > 0$ while $\overline{\gamma}_y$ reverses sign with changes in latitude. The net result is that the fine particles produce two regions toward the top of the plume where there is destruction of eddy APE, which is mainly due to $\hat{\overline{\gamma}}_{p,\bar{f}}$ (see Fig. 4b).

6. Concluding remarks

We have extended Thorncroft and Hoskins (1994b) and Grogan et al. (2016) by examining the direct radiative effects of Saharan mineral dust (SMD) aerosols on the nonlinear evolution of the AEJ–AEW system. Numerical experiments were carried out using a simplified version of the Weather Research and Forecasting (WRF) Model coupled to an online dust model. The initial states for the zonally averaged wind, potential temperature, and SMD were chosen consistent with observations. Energetics and EP flux diagnostics show that the SMD significantly affect the strength, structure, and location of the AEJ and the life cycles of the AEWs.

The numerical results show that the SMD-modified AEW life cycles are characterized by enhanced linear growth rate, weakened nonlinear stabilization, larger peak amplitude, and smaller long-time amplitude. The larger amplitudes are due to the SMD-enhanced global conversions of barotropic and baroclinic energy and the SMD generation of eddy APE. During linear growth, the local generation of eddy APE by the SMD field ($\overline{\mathrm{GE}}$) is maximized where the maximum in the mean meridional SMD gradient and critical surface are coincident—a result that was predicted by an analytical expression for $\overline{\mathrm{GE}}$ derived by Grogan et al. (2016). As the AEWs evolve in the nonlinear stabilization stage and beyond, the region occupied by $\overline{\mathrm{GE}} > 0$ decreases, while the regions occupied by $\overline{\mathrm{GE}} < 0$ increase at the base and top of the plume. This redistribution of the generation and destruction regions of eddy APE by the SMD field is due to the discrimination that takes place between the different SMD particle sizes; the finer particles remain lofted and meridionally expand while the coarser particles gravitationally settle toward the surface.

Throughout the AEW life cycle, the SMD-modified AEJ is elevated and has stronger peak winds. The SMD enhances both the EP flux divergence and the residual-mean meridional circulation, which generally oppose each other throughout the AEW life cycle. Initially, the SMD-modified residual-mean circulation accelerates the flow, but EP flux divergence quickly becomes dominant and remains so. The SMD-modified EP fluxes more rapidly decelerate the AEJ and shift its axis farther equatorward during the linear growth and nonlinear stabilization stages. The peak AEW amplitude and

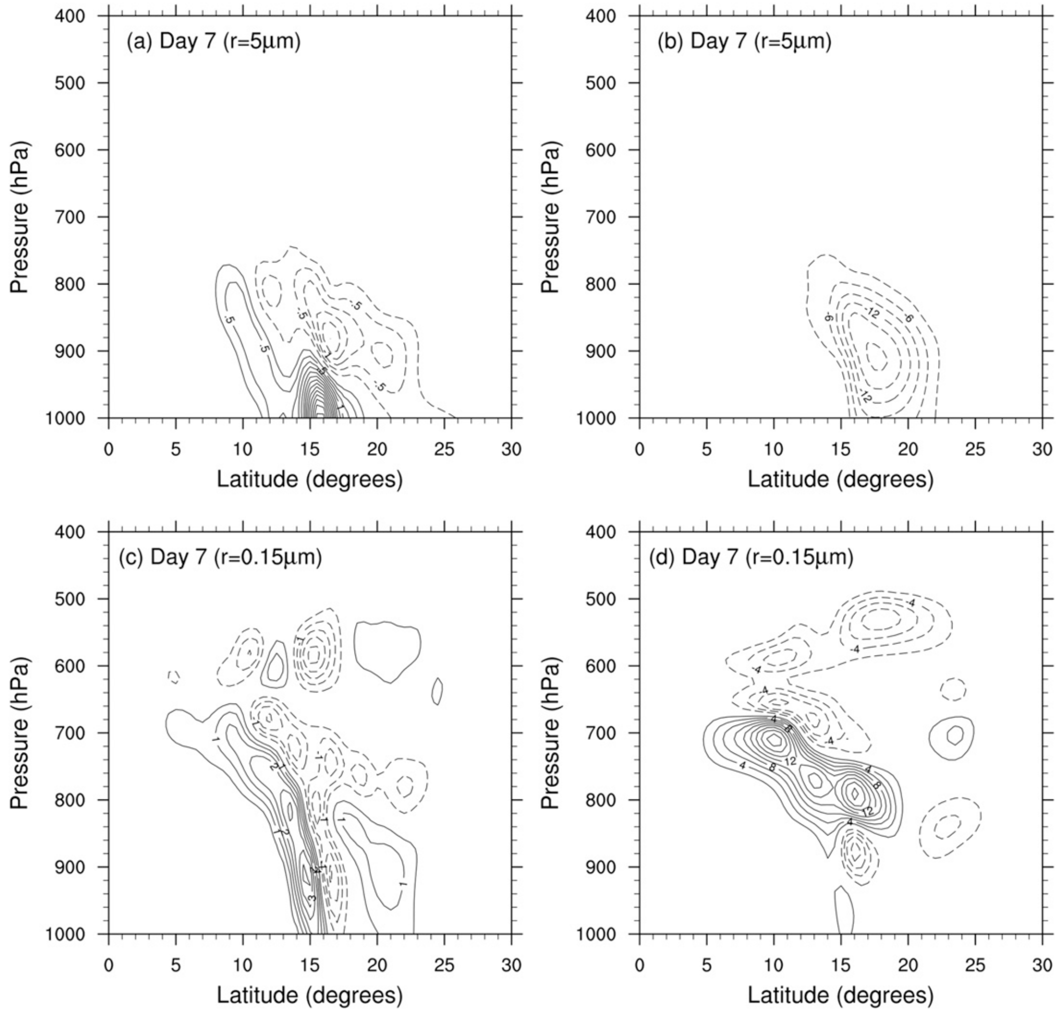

FIG. 16. The quantities (left) $\widehat{\widehat{\gamma}}_{y,\bar{j}}$ and (right) $\widehat{\widehat{\gamma}}_{p,\bar{j}}$ on day 7 for (a),(b) the coarsest SMD particle and (c),(d) the finest SMD particle. The particle radius is shown in each figure. Positive contours (solid) represent the generation of APE by the SMD particles; negative (dashed) contours represent the destruction of eddy APE. Contour intervals are (a) $0.25 \times 10^{-14}\,\mathrm{m\,K\,s^{-2}}$, (b) $3 \times 10^{-14}\,\mathrm{K^2\,Pa^{-1}}$, (c) $0.5 \times 10^{-14}\,\mathrm{m\,K\,s^{-2}}$, and (d) $2 \times 10^{-14}\,\mathrm{K^2\,Pa^{-1}}$.

reacceleration of the AEJ occur 1 day earlier than in the SMD-free case. During the AEW decay stage, the SMD-modified AEJ rebuilds as in the SMD-free case, but unlike the SMD-free case, the peak zonally averaged winds are ~20% stronger. Away from the peak winds, the EP flux divergence dominates the structural changes to the AEJ. The SMD-modified wave driving enhances the surface winds, increases the meridional and vertical shear on the periphery of the AEJ, and shifts the AEJ axis even farther equatorward.

Our results provide a foundation upon which future studies can build. For instance, an important process that we have excluded from our study is moist convection, which other studies have found can play an important role in the evolution of the AEJ–AEW system (Mekonnen et al. 2006; Cornforth et al. 2009; Poan et al. 2015). Cornforth et al. (2009) showed, for example, that moist convective processes, like the SMD examined in this study, increase the growth rate of AEWs. In contrast to the SMD, however, Cornforth et al. (2009) found that on average the moist convection weakens the AEJ, shifts its axis poleward during AEW growth, and produces long-time vacillations that trigger periodic rainfall similar to observed intraseasonal rainfall over northwestern Africa. In light of our results and those of Cornforth et al. (2009), a logical next step would be to combine SMD and moist convective processes to examine their joint influence on the AEJ–AEW system. Of particular importance would be to examine the competition between the SMD shifting the AEJ southward and the moist convection shifting it northward. Further complicating the competition is SMD microphysics: the

SMD can act as both ice nuclei and cloud condensation nuclei, which together can affect in-cloud processes (Cheng et al. 2007; Cheng et al. 2010; Klüser and Holzer-Popp 2010), while cloud downdrafts and rainfall affect the transport, emission, and deposition of SMD [Knippertz and Todd (2012), and references therein].

We based our experiments on initial climatological (zonally averaged) distributions for the AEJ and SMD. Observations show, however, that the AEJ and SMD vary temporally and spatially on intraseasonal and interannual time scales (Grist 2002; Schwanghart and Shütt 2008; Dezfuli and Nicholson 2011; Evan et al. 2016). Moreover, previous SMD-free modeling studies have shown that the structure of the AEJ can affect the life cycles of AEWs (Thorncroft 1995). Thus, further work is needed to determine how various combinations of initial AEJ structures and SMD distributions combine to affect the evolution of the AEJ–AEW system. For example, are there combinations of AEJ structure and SMD distribution that optimize the growth of AEWs or perhaps suppress AEW activity entirely? How might an internally generated SMD plume, rather than an initially imposed one, affect the AEW life cycle? And to what extent would the AEW life cycles change if zonally asymmetric rather than zonally symmetric AEJs were considered?

Hall et al. (2006) have shown, for example, that realistic, zonally asymmetric AEJs together with modest damping neutralize AEWs. Moreover, Hall et al. (2006) and subsequently Thorncroft et al. (2008) conclude that the barotropic–baroclinic instability of the AEJ alone cannot explain the generation of AEWs and assert that a convective triggering mechanism upstream of the AEJ in East Africa may be needed. Slightly downstream of this triggering region is the Bodélé depression (~17°N, 18°E), which is one of the largest SMD source regions in North Africa (Engelstaedter and Washington 2007). As the triggered waves move downstream, it is unclear how they will respond to both the SMD emissions from the Bodélé depression and to the SMD-induced changes in the zonally asymmetric AEJ itself. For this reason, and since previous SMD-free studies (Kiladis et al. 2006; Leroux and Hall 2009; Diaz and Aiyyer 2015) have shown that a zonally asymmetric background state can have an important effect of the growth of AEWs, it will be important to extend this study to background states characterized by AEJs and background SMD distributions that are zonally asymmetric.

Acknowledgments. The authors thank Emily Bercos-Hickey and William Turner IV for their comments on the manuscript. We also acknowledge high-performance computing support from Yellowstone (ark:/85065/d7wd3xhc) provided by NCAR's Computational and Information Systems Laboratory. This work was supported by NSF Grant 1321720 and by NSF Graduate Research Fellowship Grant 1524767 (D. Grogan).

REFERENCES

Andrews, D. G., and M. E. McIntyre, 1976: Planetary waves in horizontal and vertical shear: The generalized Eliassen–Palm relation and the mean zonal acceleration. *J. Atmos. Sci.*, **33**, 2031–2048, doi:10.1175/1520-0469(1976)033<2031:PWIHAV>2.0.CO;2.

Burpee, R. W., 1972: The origin and structure of easterly waves in the lower troposphere of North Africa. *J. Atmos. Sci.*, **29**, 77–90, doi:10.1175/1520-0469(1972)029<0077:TOASOE>2.0.CO;2.

Carlson, T. N., and C. B. Benjamin, 1980: Radiative heating rates for Saharan dust. *J. Atmos. Sci.*, **37**, 193–213, doi:10.1175/1520-0469(1980)037<0193:RHRFSD>2.0.CO;2.

Chen, S.-H., S.-H. Wang, and M. Waylonis, 2010: Modification of Saharan air layer and environmental shear over the Eastern Atlantic Ocean by dust-radiation effects. *J. Geophys. Res.*, **115**, D21202, doi:10.1029/2010JD014158.

——, Y.-C. Liu, T. R. Nathan, C. Davis, R. Torn, N. Sowa, C.-T. Cheng, and J.-P. Chen, 2015: Modeling the effects of dust-radiative forcing on the movement of Hurricane Helene (2006). *Quart. J. Roy. Meteor. Soc.*, **141**, 2563–2570, doi:10.1002/qj.2542.

Cheng, C.-T., W.-C. Wang, and J.-P. Chen, 2007: A modeling study of aerosol impacts on cloud microphysics and radiative properties. *Quart. J. Roy. Meteor. Soc.*, **133**, 283–297, doi:10.1002/qj.25.

——, ——, and ——, 2010: Simulation of the effects of increasing cloud condensation nuclei on mixed-phase clouds and precipitation of a front system. *Atmos. Res.*, **96**, 461–476, doi:10.1016/j.atmosres.2010.02.005.

Chou, M.-D., and M. J. Suarez, 1999: A solar radiation parameterization for atmospheric studies. NASA Tech. Memo. 104606, Vol. 15, 40 pp. [Available online at https://gmao.gsfc.nasa.gov/pubs/docs/Chou136.pdf.]

——, ——, X.-Z. Liang, and M. M.-H. Yan, 2001: A thermal infrared radiation parameterization for atmospheric studies. NASA Tech. Memo. 104606, Vol. 19, 102 pp. [Available online at https://gmao.gsfc.nasa.gov/pubs/docs/Chou137.pdf.]

Colarco, P. R., E. P. Nowottnick, C. A. Randles, B. Yi, P. Yang, K.-M. Kim, J. A. Smith, and C. G. Bardeen, 2014: Impact of radiatively interactive dust aerosols in the NASA GEOS-5 climate model: Sensitivity to dust particle shape and refractive index. *J. Geophys. Res. Atmos*, **119**, 753–786, doi:10.1002/2013JD020046.

Cornforth, R. J., B. J. Hoskins, and C. D. Thorncroft, 2009: The impact of moist processes on the African easterly jet—African easterly wave system. *Quart. J. Roy. Meteor. Soc.*, **135**, 894–913, doi:10.1002/qj.414.

Cuesta, J., J. H. Marsham, D. J. Parker, and C. Flamant, 2009: Dynamical mechanisms controlling the vertical redistribution of dust and the thermodynamic structure of the West Saharan atmospheric boundary layer during summer. *Atmos. Sci. Lett.*, **10**, 34–42, doi:10.1002/asl.207.

Dezfuli, A. K., and S. E. Nicholson, 2011: A note on long-term variations of the African easterly jet. *Int. J. Climatol.*, **31**, 2049–2054, doi:10.1002/joc.2209.

Diaz, M., and A. Aiyyer, 2015: Absolute and convective instability of the African easterly jet. *J. Atmos. Sci.*, **72**, 1805–1826, doi:10.1175/JAS-D-14-0128.1.

Edmon, H. J., B. J. Hoskins, and M. E. McIntyre, 1980: Eliassen–Palm cross sections for the troposphere. *J. Atmos. Sci.*, **44**, 1559–1573, doi:10.1175/1520-0469(1980)037<2600:EPCSFT>2.0.CO;2.

Engelstaedter, S., and R. Washington, 2007: Atmospheric controls on the annual cycle of North African dust. *J. Geophys. Res.*, **112**, D03103, doi:10.1029/2006JD007195.

Evan, A. T., C. Flamant, M. Gaetani, and F. Guichard, 2016: The past, present and future African dust. *Nature*, **531**, 493–495, doi:10.1038/nature17149.

Fielder, S., K. Schepanski, B. Heinold, P. Knippertz, and I. Tegen, 2013: Climatology of nocturnal low-level jets over North Africa and implications for modeling mineral dust emission. *J. Geophys. Res. Atmos.*, **118**, 6100–6121, doi:10.1002/jgrd.50394.

Grist, J. P., 2002: Easterly waves over Africa. Part I: The seasonal cycle and contrasts between wet and dry years. *Mon. Wea. Rev.*, **130**, 197–211, doi:10.1175/1520-0493(2002)130<0197:EWOAPI>2.0.CO;2.

Grogan, D. F. P., T. R. Nathan, and S.-H. Chen, 2016: Effect of Saharan dust on the linear dynamics of African easterly waves. *J. Atmos. Sci.*, **73**, 891–911, doi:10.1175/JAS-D-15-0143.1.

Hall, N. M. J., G. N. Kiladis, and C. D. Thorncroft, 2006: Three-dimensional structure and dynamics of African easterly waves. Part II: Dynamical modes. *J. Atmos. Sci.*, **63**, 2231–2245, doi:10.1175/JAS3742.1.

Holton, J. R., 2004: *An Introduction to Dynamic Meteorology*. Elsevier Academic Press, 535 pp.

Hosseinpour, F., and E. M. Wilcox, 2014: Aerosol interactions with African/Atlantic climate dynamics. *Environ. Res. Lett.*, **9**, 075004, doi:10.1088/1748-9326/9/7/075004.

Hsieh, J.-S., and K. H. Cook, 2005: Generation of African easterly wave disturbances: Relationship to the African easterly jet. *Mon. Wea. Rev.*, **133**, 1311–1327, doi:10.1175/MWR2916.1.

Jones, C., N. Mahowald, and C. Luo, 2003: The role of easterly waves on African desert dust transport. *J. Climate*, **16**, 3617–3628, doi:10.1175/1520-0442(2003)016<3617:TROEWO>2.0.CO;2.

——, ——, and ——, 2004: Observational evidence of African desert dust intensification of easterly waves. *Geophys. Res. Lett.*, **31**, L17208, doi:10.1029/2004GL020107.

Jury, M. R., and M. J. Santiago, 2010: Composite analysis of dust impacts on African easterly waves in the Moderate Resolution Imaging Spectrometer era. *Geophys. Res. Lett.*, **115**, D16213, doi:10.1029/2009JD013612.

Karyampudi, V. M., and T. N. Carlson, 1988: Analysis and numerical simulations of the Saharan air layer and its effect on easterly wave disturbances. *J. Atmos. Sci.*, **45**, 3102–3136, doi:10.1175/1520-0469(1988)045<3102:AANSOT>2.0.CO;2.

——, and Coauthors, 1999: Validation of the Saharan dust plume conceptual model using lidar, Meteosat, and ECMWF data. *Bull. Amer. Meteor. Soc.*, **80**, 1046–1075, doi:10.1175/1520-0477(1999)080<1045:VOTSDP>2.0.CO;2.

Kiladis, G. N., C. D. Thorncroft, and N. M. J. Hall, 2006: Three-dimensional structure and dynamics of African easterly waves. Part I: Observations. *J. Atmos. Sci.*, **63**, 2212–2230, doi:10.1175/JAS3741.1.

Klüser, L., and T. Holzer-Popp, 2010: Relationships between mineral dust and cloud properties in the West African Sahel. *Atmos. Chem. Phys.*, **10**, 6901–6915, doi:10.5194/acp-10-6901-2010.

Knippertz, P., and M. C. Todd, 2012: Mineral dust aerosols over the Sahara: Meteorological controls on emission and transport and implication for modeling. *Rev. Geophys.*, **50**, RG1007, doi:10.1029/2011RG000362.

Kok, J. F., 2011: A scaling theory for the size distribution of emitted dust aerosols suggests climate models underestimate the size of the global dust cycle. *Proc. Natl. Acad. Sci. USA*, **108**, 1016–1021, doi:10.1073/pnas.1014798108.

Konare, A., A. S. Zakey, F. Solmon, F. Giorgi, S. Rauscher, S. Ibrah, and X. Bi, 2008: A regional climate modeling study of the effect of desert dust on the West African monsoon. *J. Geophys. Res.*, **113**, D12206, doi:10.1029/2007JD009322.

Leroux, S., and N. M. J. Hall, 2009: On the relationship between African easterly waves and the African easterly jet. *J. Atmos. Sci.*, **66**, 2303–2316, doi:10.1175/2009JAS2988.1.

Ma, P.-L., K. Zhang, J. J. Shi, T. Matsui, and A. Arking, 2012: Direct radiative effect of mineral dust on the development of African easterly waves. *J. Appl. Meteor. Climatol.*, **51**, 2090–2104, doi:10.1175/JAMC-D-11-0215.1.

Mekonnen, A., C. D. Thorncroft, and A. R. Aiyyer, 2006: Analysis of convection and its association with African easterly waves. *J. Climate*, **19**, 5405–5421, doi:10.1175/JCLI3920.1.

Merkine, L.-O., 1978: A note on the finite amplitude dynamics of spatially growing baroclinic waves on an *f*-plane. *Tellus*, **30**, 477–486, doi:10.1111/j.2153-3490.1978.tb00865.x.

Miller, R. L., and I. Tegen, 1998: Climate response to soil dust aerosols. *J. Climate*, **11**, 3247–3267, doi:10.1175/1520-0442(1998)011<3247:CRTSDA>2.0.CO;2.

Moulin, C., and I. Chiapello, 2004: Evidence of the control of summer atmospheric transport of African dust over the Atlantic by Sahel source from TOMS satellites (1979–2000). *Geophys. Res. Lett.*, **31**, L02107, doi:10.1029/2003GL018931.

Nathan, T. R., 1993: Nonlinear evolution of spatially growing baroclinic waves. *Geophys. Astrophys. Fluid Dyn.*, **68**, 15–35, doi:10.1080/03091929308203560.

——, 1998: Nonlinear spatial baroclinic instability in slowly varying zonal flow. *Dyn. Atmos. Oceans*, **27**, 81–90, doi:10.1016/S0377-0265(97)00002-X.

Norquist, D. C., E. E. Recker, and R. J. Reed, 1977: The energetics of African wave disturbances as observed during phase III of GATE. *Mon. Wea. Rev.*, **105**, 334–342, doi:10.1175/1520-0493(1977)105<0334:TEOAWD>2.0.CO;2.

Pedlosky, J., 1970: Finite amplitude baroclinic waves. *J. Atmos. Sci.*, **27**, 15–30, doi:10.1175/1520-0469(1970)027<0015:FABW>2.0.CO;2.

——, 1987: *Geophysical Fluid Dynamics*. Springer, 710 pp.

Poan, D. E., J.-P. Lafore, R. Roehrig, and F. Couvreux, 2015: Internal processes within the African easterly wave system. *Quart. J. Roy. Meteor. Soc.*, **141**, 1121–1136, doi:10.1002/qj.2420.

Reale, O., K. M. Lau, and A. da Silva, 2011: Impact of an interactive aerosol on the African easterly jet in the NASA GOES-5 global forecasting system. *Wea. Forecasting*, **26**, 504–519, doi:10.1175/WAF-D-10-05025.1.

Reed, R. J., D. C. Norquist, and E. E. Recker, 1977: The structure and properties of African wave disturbances as observed during phase III of GATE. *Mon. Wea. Rev.*, **105**, 317–333, doi:10.1175/1520-0493(1977)105<0317:TSAPOA>2.0.CO;2.

——, E. Klinker, and A. Hollingsworth, 1988: The structure and characteristics of African easterly wave disturbances as determined from the ECMWF operational analysis/forecast system. *Meteor. Atmos. Phys.*, **38**, 22–33, doi:10.1007/BF01029944.

Schwanghart, W., and B. Schütt, 2008: Meteorological causes of Harmattan dust in West Africa. *Geomorphology*, **95**, 412–428, doi:10.1016/j.geomorph.2007.07.002.

Thorncroft, C. D., 1995: An idealized study of African easterly waves. III: More realistic basic states. *Quart. J. Roy. Meteor. Soc.*, **121**, 1589–1614, doi:10.1002/qj.49712152706.

——, and B. J. Hoskins, 1994a: An idealized study of African easterly waves. I: Linear theory. *Quart. J. Roy. Meteor. Soc.*, **120**, 953–982, doi:10.1002/qj.49712051809.

——, and ——, 1994b: An idealized study of African easterly waves. II: A nonlinear view. *Quart. J. Roy. Meteor. Soc.*, **120**, 983–1015, doi:10.1002/qj.49712051810.

——, and K. Hodges, 2001: African easterly wave variability and its relationship to Atlantic tropical cyclone activity. *J. Climate*, **14**, 1166–1179, doi:10.1175/1520-0442(2001)014<1166:AEWVAI>2.0.CO;2.

——, N. M. J. Hall, and G. N. Kiladis, 2008: Three-dimensional structure and dynamics of African easterly waves. Part III: Genesis. *J. Atmos. Sci.*, **65**, 3596–3607, doi:10.1175/2008JAS2575.1.

Tompkins, A. M., C. Cardinali, J.-J. Morcette, and M. Rodwell, 2005: Influence of aerosol climatology on forecasts of the African easterly jet. *Geophys. Res. Lett.*, **32**, L10801, doi:10.1029/2004GL022189.

Trenberth, K. E., 1986: An assessment of the impact of transient eddies on the zonal flow during a blocking episode using localized Eliassen–Palm flux diagnostics. *J. Atmos. Sci.*, **43**, 2070–2087, doi:10.1175/1520-0469(1986)043<2070:AAOTIO>2.0.CO;2.

Tulet, P., M. Mallet, V. Pont, J. Pelon, and A. Boone, 2008: The 7–13 March 2006 dust storm over West Africa: Generation, transport, and vertical stratification. *J. Geophys. Res.*, **113**, D00C08, doi:10.1029/2008JD009871.

Westphal, D. L., O. B. Toon, and T. N. Carlson, 1988: A case study of mobilization and transport of Saharan dust. *J. Atmos. Sci.*, **45**, 2145–2175, doi:10.1175/1520-0469(1988)045<2145:ACSOMA>2.0.CO;2.